AIAA JOURNAL
Vol. 51, No. 12, December 2013

Two-Dimensional Model for Liquid-Rocket Transverse Combustion Instability

William A. Sirignano* and Pavel P. Popov†
University of California, Irvine, California 92697

DOI: 10.2514/1.J052512

Nonlinear, transverse-mode, liquid-propellant-rocket-motor combustion instability is examined with a two-dimensional model. The three-dimensional equations are integrated over the axial direction, for a multi-orifice short nozzle. Nonlinear transverse-wave oscillations in the circular combustion chamber are examined with the primary flow in the axial direction. Turbulent mixing of methane and gaseous oxygen with coaxial injection is analyzed. The combustion has two characteristic times, one for mixing and the other for chemical kinetics, producing a time lag in the energy-release rate relative to pressure. Then, the coupled combustion process and wave dynamics are calculated for a 10-injector chamber with methane and gaseous-oxygen propellants. The linear first tangential mode is imposed initially. Nonlinear triggering occurs; above a critical initial amplitude, the amplitude grows; otherwise, it decays with time. The second tangential mode also develops, and the nonlinear resonance creates a subharmonic mode with a frequency equal to the difference between the two tangential-mode frequencies. A modification of the characteristic times leads to a triggered instability, in which the first tangential mode transfers energy to its harmonics without the appearance of the second tangential mode or the subharmonic mode. Local pulses of pressure and velocity can also trigger instabilities with a strong sensitivity to the direction of the pulse.

Nomenclature

$\mathbf{A}$	=	chemical-rate constant, $m^3/(s \cdot kg)$
A_{entrance}	=	cross-sectional area of nozzle entrance, m^2
A_{throat}	=	cross-sectional area of nozzle throat, m^2
A, B	=	constants defined in Eq. (21)
a	=	speed of sound, m/s
a, b	=	chemical-rate constants
C	=	constant defined in Eq. (25)
c_p	=	specific heat at constant pressure, $J/K \cdot kg$
c_v	=	specific heat at constant volume, $J/K \cdot kg$
D	=	mass diffusivity, m^2/s
E	=	energy-release rate, $J/kg \cdot s$
f	=	frequency, s^{-1}
G	=	Green's function
h	=	specific enthalpy, J/kg
K, $\hat{K}$	=	constants defined in Eqs. (16) and (17)
L	=	chamber length, m
M	=	Mach number
$\dot{m}$	=	mass-flow rate, kg/s
p	=	pressure, $N \cdot m^{-2}$
R	=	chamber radius, m
$\mathbf{R}$	=	mixture specific gas constant, $J/kg \cdot K$
R_i	=	inner radius of coaxial jet, m
R_o	=	outer radius of coaxial jet, m
$\mathbf{R}_u$	=	universal gas constant, $J/kg \cdot mol \cdot K$
r	=	radial position, m
$r_{1/2}$	=	half-width of coaxial jet, m
s	=	specific entropy, $J/K \cdot kg$
T	=	temperature, K
t	=	time, s
U	=	coaxial jet velocity, m/s
$\mathbf{u}$	=	vector velocity, m/s
u_j	=	Cartesian velocity component, m/s
u_r	=	radial velocity component, m/s
u_θ	=	tangential velocity component, m/s
x_j	=	Cartesian coordinate, m
Y_i	=	mass fraction of species i

Greek symbols

α, β	=	Shvab–Zel'dovich variables
γ	=	ratio of specific heats
ϵ	=	activation energy, $J/kg \cdot mol$
θ	=	azimuthal position
κ	=	variable defined after Eq. (32)
ν	=	kinematic viscosity, m^2/s
ν_T	=	turbulent kinematic viscosity, m^2/s
ρ	=	density, $kg \cdot m^{-3}$
τ_M	=	characteristic mixing time, s
τ_R	=	characteristic reaction time, s
ϕ	=	velocity potential, m^2/s
ω_i	=	reaction rate of species i, s^{-1}

Subscripts

F	=	fuel
i	=	index for chemical species
j	=	index for Cartesian coordinates
O	=	oxidizer
0	=	undisturbed state

Presented as Paper 2013-566 at the Aerospace Sciences Meeting, Grapevine, TX, 7–10 January 2013; received 2 January 2013; revision received 29 March 2013; accepted for publication 12 April 2013; published online 2 August 2013.

*Professor, Department of Mechanical and Aerospace Engineering. Fellow AIAA.

†Postdoctoral Researcher, Department of Mechanical and Aerospace Engineering. AIAA Member.

I. Introduction

LIQUID-PROPELLANT-ROCKET-ENGINE (LPRE) combustion instability has been a long-standing natural phenomenon, which causes problems and creates the need for control. In LPRE, the combustion process produces a very high energy-release rate per unit volume which, in many circumstances, has characteristic times that result in the reinforcement of the acoustical oscillations and produces very high amplitudes. These oscillations can cause undesirable oscillations in thrust, vibrations that result in problems for people or equipment on the spacecraft, and increased heat transfer in already critical regions (e.g., the nozzle throat). Transverse spinning waves can have substantially larger amplitudes than longitudinal waves because no shock waves form and thereby dissipation is reduced. The combustion concentrates near the injector end, resulting in very high

heat-transfer rates to the injector. The increased heat transfer at the injector and/or nozzle throat often leads to the destruction of those wall materials and disaster for the flight mission.

Theoretical, computational, and experimental research has been underway at varying levels of intensity for more than a half-century. Here, the history of theoretical and computational research will be briefly reviewed, followed by an explanation of the new methods and new goals in this current research. Important historical efforts on solid-propellant combustion and other combustion engines will not be discussed because the physics are different and brevity is desirable. Most of the physics of the oscillations were identified in the 1950s and 1960s, but the knowledge of the details of coupling with the combustion processes has trailed. An excellent compilation of major research during that early period is provided by Harrje and Reardon [1]. Also, an interesting discussion of the famous F-1 rocket-motor instability problems is given by Oefelein and Yang [2]. Two types of instability occur: linear or spontaneous instability and nonlinear or triggered instability. The describing terms pertain to initiation only; all instabilities of concern have nonlinear behavior once established. Linear instabilities grow in amplitude from the normal noise associated with the high mass-flow multi-injector rocket-chamber environment; theoretically, they grow from infinitesimal disturbances. Nonlinear instabilities require a disturbance of sufficient magnitude to overcome a required threshold. Without such a disturbance, linear stability is exhibited. A disruption in propellant mass flow or a very large fluctuation caused by transient operation can provide the necessary trigger. In experiments, the use of small explosives has triggered instabilities. Both types are addressed in the current work, but a triggered instability presents the greater challenge and is emphasized here.

The longitudinal-mode linear instability was addressed extensively by Crocco and Cheng [3,4]. The two-parameter (n, τ) coupling between combustion and acoustics was developed along with the first method for superposition of two continua for two phases (condensed phase and gas) for any application. The sensitive time-lag theory was the foundation of the description of the combustion response to and reinforcement of the acoustic oscillations. It avoided a detailed description of the unsteady combustion process with the intent that the two parameters n and τ, which were independent of oscillation frequency, could be determined empirically through experiments. On this foundation, the theory of longitudinal oscillations with modifications due to mass, momentum, and energy exchanges between the phases was established. The early work of Tsien [5] on the acoustical reflections in the nozzle and handling of the throat singularity was extended with experimental verification. The nozzle oscillation analysis was later extended to address three-dimensional (3-D) linear oscillations in rocket motors [6,7]. Sirignano and Crocco [8] and Sirignano [9] showed the existence of both unstable and stable limit-cycle oscillations for the longitudinal mode, sometimes with shock-wave formation. The unstable limit cycle gives identification of a threshold for triggering: below this amplitude, disturbances decay to zero amplitude in time, whereas above it, growth to larger amplitude occurs. The theory was later extended for longitudinal modes [10,11] and for transverse modes [12].

A theoretical prediction of triggering was first given by Sirignano [9] for the longitudinal mode, followed by Zinn [12] for the transverse mode. The approach predicts either a stable or unstable limit cycle for each point in the n, τ plane near the linear-stability limit line. See, for example, Fig. 1, which describes the longitudinal mode. The upper plots show linear limit curves and define displacement from the linear limits. The lower plots show nonlinear limit-cycle amplitudes as a function of displacement. These early pioneering efforts on nonlinear triggering did not predict the expected higher-amplitude stable limit cycle in the n, τ domains, where an unstable limit cycle and nonlinear triggering were predicted. Presumably, if the analyses were extended sufficiently beyond third-order terms in the amplitude parameter, the stable limit cycle would be determined.

The amplitude parameter ε grows as a quadratic function of the distance from the linear-stability line. If it extends over the linear stable region, it gives the amplitude for an unstable limit cycle and indicates that triggering occurs when a disturbance has an amplitude that exceeds that threshold value, as shown in the lower-left portion of Fig. 1. If it extends over the linearly unstable region, it gives the amplitude for a stable limit cycle toward which a very small disturbance grows and reaches after several periods of oscillation, as shown in the lower-right portion of Fig. 1. Later, Mitchell et al. [10]

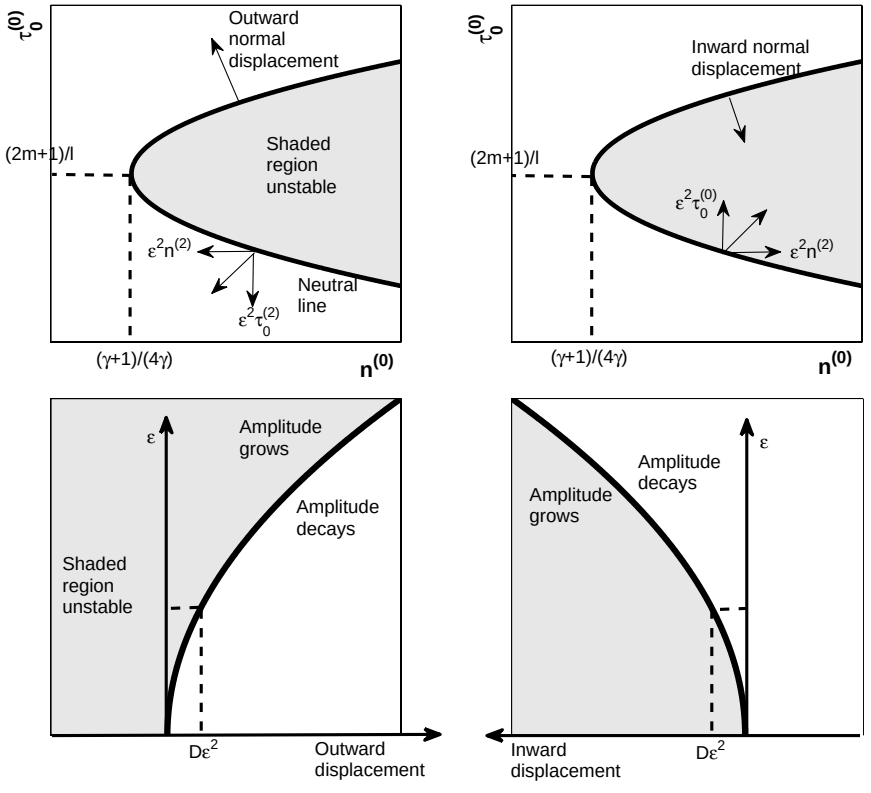

Fig. 1 Stability limits in the n, τ domain.

improved the approach for the longitudinal-mode analysis so that, for triggered cases, both the unstable and stable limit cycles were predicted, and the region of triggering was more clearly defined. The stable limit cycle contained a shock-wave discontinuity. For a portion of the parameter domain, the unstable limit cycle also had a shock-wave instability. See Fig. 2. The peak-to-peak and shock amplitudes are portrayed for both stable and unstable limit cycles.

The early nonlinear analyses coming from previous works relied on singular perturbation techniques, which were extensions of Poincare's method. Zinn and Powell [13] introduced the Galerkin method to the field, still using the n, τ methods. It had the advantages that the resulting ordinary differential equations reduced the computational complexity, and transient behavior could be analyzed in addition to the limit-cycle behavior. Also, it offered the ability to account for the nonlinear transfer of energy between different natural modes of instability. Some researchers, in a series of papers beginning in the 1970s, used an eigenfunction expansion together with a two-time-variable technique that had some of the same advantages; see Awad and Culick [14], Yang et al. [15], and Culick [16,17]. More recently, there is work with a Galerkin approach (also known as reduced-basis modeling) by Flandro et al. [18] and Jacob et al. [19]. Haddad and Majdalani [20] considered the effects of wall boundary layers on the acoustics following a similar approach. Perturbation methods and Galerkin methods require some a priori knowledge of the relevant modes of oscillation. The elegant asymptotics of the two-time-variable method becomes less useful when many modes with a range of timescales are involved.

The aforementioned analyses generally used heuristic methods rather than a first-principles approach to describe the combustion process; in particular, either the sensitive time-lag theory with the n, τ parameters or an approach with the gain and phase parameters. (Note that these two systems could be equated to the linear order. That is, the two parameters of one system could be easily related to the two parameters of the other system and frequency.) The exception to the heuristic approach was the work by Sirignano and Crocco [8], which used a simplistic chemical rate. Over several decades, some progress was made in understanding the driving mechanisms of the LPRE instability for subcritical and transcritical operations, in which vaporization is rate controlling [21–34]. Supercritical operation presents a very different situation whereby no distinction between phases occurs. The results here will address situations in which the propellants are injected as gas. These propellants could have been used for gas generation to drive a turbo pump or as a coolant before injection. Or, they could have been injected at supercritical conditions. Therefore, the mixing and chemical-reaction model discussed later will apply to gases only. The wave-dynamics model presented later could be used for cases with injection of liquids if terms were added to account for the exchange of momentum between the phases. In that way, some vaporization models identified previously could be coupled with the wave-dynamics model here in the following analysis.

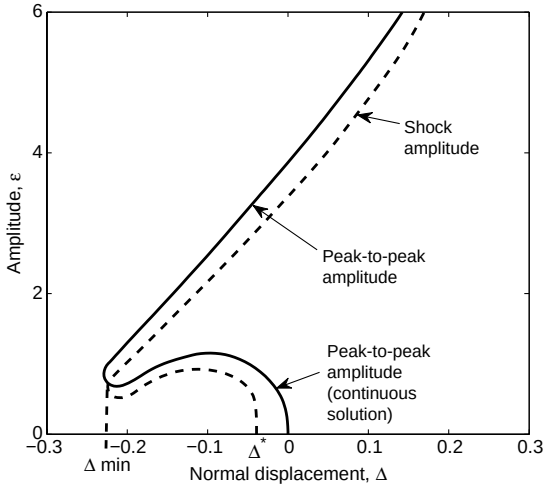

Fig. 2 Schematic of nonlinear limit-cycle amplitudes found by Mitchell et al. [10].

There are two general types of acoustical combustion instability: driven instability and self-excited instability, as noted by Culick [17]. He describes evidence in some solid-propellant rockets of the former (driven) type, in which noise or vortex shedding (a more organized noise) causes kinematic waves (i.e., waves carried with the moving gas) of vorticity or entropy to travel to some point where an acoustical reflection occurs. The reflected wave causes more noise or vortex shedding after traveling back and a cyclic character results. These driven types do not rely on acoustical chamber resonance, and acoustical waves traveling upstream are the only type of consequence with kinematic waves only traveling downstream by the kinematic definition. They are much smaller in amplitude because the energy level is limited by the driving energy. This type of instability has also been observed in ramjet combustors, but never in liquid rockets. Therefore, they will not be addressed in this proposed research.

Self-excited instabilities are the primary type relevant to liquid-propellant rockets. These types are not limited in amplitude by the energy of the initiation action; they find the energy within their own macrobehavior as the oscillations grow and develop. Thus, the initiation is microlevel, but the instability becomes macrolevel. These instabilities include those linear unstable situations, in which normal low-level engine noise is sufficient to initiate the instability oscillation, and those triggered instabilities, which require a larger initial disturbance to initiate the nonlinear oscillation. Physically, the rogue disturbance is some deviant behavior in the operation that has uncertainty with regard to location in the physical coordinates, duration, and magnitude. The deviant behavior jolts the steady-state behavior. Sometimes, there is a recovery and a return to the steady state, but, at other times, the development of the oscillation occurs with a growing of the oscillation amplitude until the limit cycle is reached.

For the driven instability, the noise or disturbance terms determine the final oscillatory behavior. If the noise were eliminated, that type of instability disappears. For the instability of liquid rocket motors, moderate (normal steady-state rumbling) noise might initiate the linear instability in certain operational domains, and large disruptive noise (e.g., small bomb or large operational change) might trigger the nonlinear instability in some other operational domain. In those cases, noise or disruptions are only initiators with modest energy levels compared to the energy of the ultimate oscillation. The initiators can be turned off once the instability starts, and the oscillation will remain and grow. That is, it becomes driven by a coupling between combustion and acoustics. The stochastic nature pertains only to the initiation mechanism, which moves the dynamics from the steady state (or nonoscillatory starting transient) to a stable limit cycle (the periodic or chaotic nonlinear oscillation). The limit cycles and the equilibrium points are neither stochastic in nature nor stochastic with regard to the ultimate driving mechanism.

The instability mechanism is made further complex due to the possible injector-to-injector interactions and interactions with the feed system and upstream manifold. Thus, to understand the source and result of perturbation with the consequent instability mechanism, the rocket motor, with its very large number of propellant-injector streams, must be treated as a complex system. Each of these streams can be viewed as a component with semi-autonomy but strong coupling with other streams. The complex systems contain 1) many building blocks that can be considered as semi-autonomous components or subsystems, 2) connectivity (networking) among the complex-system components, 3) a multiscale structure, 4) a self-organizing capability such that the overall structure and behavior are not deducible as merely the sum of its building blocks (nonlinear synergism among the components is vital) and macrolevel behavior can emerge from the interactions among the components, and 5) unpredictable behavior that includes chaotic behavior. Therefore, the characteristics of a complex system can be seen in the liquid-propellant rocket motor. The key knowledge areas for addressing complex systems can include nonlinear dynamics, statistics, networks, optimization, multi-agent-based simulation, and the many

subareas of these fields [35–46]. Of course, combustion dynamics are a rich and challenging subarea of nonlinear dynamics.

Each injector stream in the rocket-motor system can be viewed as a component of such a complex system with a degree of autonomy but strongly networked. An individual component can exhibit a behavior that creates a certain structure, which eventually has a global consequence for the system.

There have been many studies of nonlinear combustion instability that relate to solid-propellant rocket motors, ramjet engines, gas-turbine engines, and industrial furnaces, which will not be discussed in any detail here. However, note that there has been no prediction or experimental evidence of triggering in those devices. See, for example, the nonlinear analyses of solid rockets [47,48], of a chemical-rate-controlled gaseous rocket [8], and of the ramjet combustor [30], each of which predicts only the stable limit cycles.

Experimental studies of full-scale rocket motors are often performed for final testing; however, systematic studies of combustion instability in a possible design are very difficult and perhaps not yet possible. On the other hand, numerical simulations can be used to probe and understand the rocket motor as a complex system, and to predict instability. A detailed simulation of combustion stability in multi-injector LPREs is computationally intensive and has only been simulated for simple configurations using advanced large-eddy-simulation (LES) techniques. There are several single-injector studies [49–58]. A systematic LES of a multi-injector system is still to be demonstrated.

The goal was to develop a model equation or a small system of equations that describe the essential features of transverse nonlinear oscillations in cylindrical combustion chambers for LPREs. The combustion chamber with its many propellant injectors and associated propellant streams will be viewed as a complex system, in which these injectors and streams are networked, but yet have some degree of local autonomy.

There is a special interest in studying the nonlinear triggering phenomenon, using a first-principles description of the combustion process. It is important to keep in the model the terms that add energy or damp oscillations or produce a major change to the wave shape. Here, for the first time, a prediction of both the stable and unstable transverse-mode limit cycles will be made in parameter domains where triggering is possible. The injected propellants will be considered as preheated and gaseous; two-phase flows can be considered in the future. While the aim is to establish a foundation for future stochastic analysis of the LPRE combustion-instability phenomenon as the behavior of a complex system, the analysis here is deterministic, and the physical phenomena are deterministic.

II. Basic Equations for Wave Dynamics

The equations will be simplified by assuming inviscid, nonheat-conducting, nonmass-diffusing flow. Turbulent fluctuations will be considered small compared to acoustic amplitudes; also, the turbulent length scales will be shorter than the acoustic wavelengths, which also allow their neglect. The turbulence is generated largely by the jets of propellants entering the combustion chamber, and the length scales are determined by transverse jet dimensions and spacing between adjacent jets. Acoustic wavelengths are determined by the much larger chamber dimensions. Other variations with length scales substantially shorter than the acoustic wavelength can be neglected. The propellants will be considered to be gaseous when injected into the combustion chamber. Mixing and chemical reaction will be modeled. Because the combustion chamber operates at supercritical pressure, a single-phase fluid will be considered. For the transverse mode, variations of amplitudes in the transverse direction will be much greater than variations in the axial direction of the cylindrical configuration. This will facilitate the reduction of the problem from a 3-D unsteady problem to a two-dimensional (2-D) unsteady formulation.

The continuity equation for the fluid gives

$$\frac{\partial \rho}{\partial t} + \nabla \cdot (\rho \mathbf{u}) = 0 \tag{1}$$

and the vector momentum equation for the fluid is

$$\frac{\partial (\rho \mathbf{u})}{\partial t} + \nabla \cdot (\rho \mathbf{u}\mathbf{u}) + \nabla p = 0 \tag{2}$$

in which ρ is the density, p is the pressure, and the vector velocity $\mathbf{u}$ has three components. Gravity and viscosity are neglected.

The energy equation may be written as follows:

$$\frac{\partial (\rho h_s)}{\partial t} + \nabla \cdot (\rho \mathbf{u} h_s) - \frac{\partial p}{\partial t} = E \tag{3}$$

in which $h_s = h + \mathbf{u} \cdot \mathbf{u}/2$; h is the specific enthalpy, h_s is the specific stagnation enthalpy, and E is the time rate of energy per unit volume, which is converted from a chemical form to a thermal form.

A perfect gas and constant specific heats are assumed. Of course, at the very high pressures, there should be corrections to the gas law, and, at the high temperatures, the specific heats should be variable. The approximation is expected to preserve the quality of the wave dynamics and the combustion dynamics, and not hide any primary physics. Quantitative adjustments can be considered later. It follows that

$$p = \rho \mathbf{R} T = \left(\sum_{n=1}^{N} Y_n \mathbf{R}_n \right) \rho T \tag{4}$$

$$a^2 = \gamma R T \tag{5}$$

$$\frac{s}{c_v} = \gamma \ln T - (\gamma - 1) \ln p \tag{6}$$

in which $\mathbf{R}$ is the specific gas constant for the mixture of gases in the chamber; Y_n and $\mathbf{R}_n$ are the mass fraction and specific gas constant, respectively, for the nth species in the fluid mixture; T is the gas temperature; a is the speed of sound; s is the specific entropy; c_p is the specific heat at constant pressure; c_v is the specific heat at constant volume; and $\gamma = c_p/c_v$.

A. Three-Dimensional Wave Equation

The development of a wave equation begins by subtracting the divergence of the momentum equation (2) from the time derivative of the continuity equation (1). This yields

$$\frac{\partial^2 \rho}{\partial t^2} - \nabla^2 p = \nabla \cdot [\nabla \cdot (\rho \mathbf{u}\mathbf{u})] \tag{7}$$

Neglect of the variation of the gas constant $\mathbf{R}$ due to the multicomponent nature of the fluid, differentiation of Eq. (4), substitution from Eq. (3) for enthalpy, differentiation again with respect to the time, reorganization of the equation, use of the combined first and second laws of thermodynamics to write $\rho \nabla h = \nabla p + \rho T \nabla s$, and substitution for ∇h yields

$$a^2 \frac{\partial^2 \rho}{\partial t^2} = \frac{\partial^2 p}{\partial t^2} - \frac{\partial \rho}{\partial t}\frac{\partial a^2}{\partial t} - (\gamma - 1)\frac{\partial E}{\partial t} + (\gamma - 1)\frac{\partial}{\partial t}\left[\frac{D(\mathbf{u} \cdot \mathbf{u})/2}{Dt} + \mathbf{u} \cdot \nabla p + \rho T \mathbf{u} \cdot \nabla s \right] \tag{8}$$

Neglect is made of entropy gradients in the flow for the purpose of developing a model equation. One can assume that fine-scale mixing eliminates these entropy gradients. This removes the last term of the preceding equation. The previous two terms can be shown to cancel each other by taking the dot product of velocity $\mathbf{u}$ with Eq. (2). The length scales for transverse gradients of entropy, other scalar properties, and vorticity are of the order of the injector diameter, the order of spacing between adjacent injectors, or smaller. These dimensions are smaller than the common wavelengths of oscillations in the combustion chamber. Also, these properties advect and diffuse, but are not propagated by acoustic waves. Turbulent mixing will

uniformize these quantities rapidly, whereas acoustical pressure and velocity oscillations will not be vitiated by turbulence.

Because of the sequential vector-calculus operations, tensor notation will be more convenient. The use of Cartesian coordinates will be temporary; after obtaining the 2-D model equation, a switch to cylindrical polar coordinates will be made. The previously described analysis yields

$$\frac{\partial^2 p}{\partial t^2} - a^2 \frac{\partial^2 p}{\partial x_j \partial x_j} = \frac{\partial \rho}{\partial t}\frac{\partial a^2}{\partial t} + (\gamma - 1)\frac{\partial E}{\partial t} + a^2 \frac{\partial^2 (\rho u_j u_i)}{\partial x_i \partial x_j} \quad (9)$$

The left-hand side of the equation represents the wave operator in three dimensions. A mild nonlinearity appears through the coefficient a^2. The first and third terms on the right-hand side are strongly nonlinear terms that are conservative, but will affect the wave shape. The second term on the right represents the influence of the energy conversion and can be a strong driver of the nonlinear oscillation.

B. Reduction to a Two-Dimensional Wave Equation

Now, a 2-D model is developed by integrating Eq. (9) over the primary flow direction, x_3. Focus is made on the transverse-mode instability, and so the major oscillations will be in the x_1 and x_2 directions. A cylindrical combustion chamber is considered with the injector at $x_3 = 0$ and the nozzle entrance at $x_3 = L$. Variations of the pressure, velocity, and other variables in the x_3 direction will be smaller than variations in other directions.

Define the 2-D average values: $\tilde{p} = (1/L)\int_0^L p\,\mathrm{d}x_3$, $\tilde{\rho} = (1/L)\int_0^L \rho\,\mathrm{d}x_3$, $\tilde{a} = (1/L)\int_0^L a\,\mathrm{d}x_3$, and $\tilde{\mathbf{u}} = (1/L)\int_0^L \mathbf{u}\,\mathrm{d}x_3$. Now, Eq. (9) is integrated over x_3, neglecting the difference between the products of averages and the averages of products:

$$\frac{\partial^2 \tilde{p}}{\partial t^2} - \tilde{a}^2 \frac{\partial^2 \tilde{p}}{\partial x_j \partial x_j} = \frac{\tilde{a}^2}{L}\left[\left.\frac{\partial p}{\partial x_3}\right|_L - \left.\frac{\partial p}{\partial x_3}\right|_0\right] + \frac{\partial \tilde{\rho}}{\partial t}\frac{\partial \tilde{a}^2}{\partial t} + (\gamma - 1)\frac{\partial \tilde{E}}{\partial t} + \tilde{a}^2 \frac{\partial^2 (\tilde{\rho}\tilde{u}_j \tilde{u}_i)}{\partial x_i \partial x_j} + \frac{\tilde{a}^2}{L}\left[\left.\frac{\partial (\rho u_j u_3)}{\partial x_j}\right|_L - \left.\frac{\partial (\rho u_j u_3)}{\partial x_j}\right|_0\right] \quad (10)$$

in which $i = 1, 2$; $j = 1, 2$.

Set to zero and ignore in Eq. (10) two terms that result from the integration of the $i = 3$; $j = 1, 2$ portions of the last term in Eq. (9), namely, the quantity

$$a^2 \frac{1}{L}\frac{\partial (\rho u_3 u_j)}{\partial x_j} \quad (11)$$

evaluated at $x = 0$ and $x = L$. These terms relate to the transverse gradient of the influx at the injector and efflux at the nozzle entrance of the transverse momentum. Assume that the injected propellant enters with no transverse momentum, and the multi-orifice nozzle (discussed as follows) eliminates transverse momentum at its entrance.

Note that, from the momentum equation (2)

$$\frac{\partial p}{\partial x_3} + \frac{\partial (\rho u_j u_3)}{\partial x_j} = -\frac{\partial (\rho u_3)}{\partial t} \quad (12)$$

which can be substituted into Eq. (10) to obtain

$$\frac{\partial^2 \tilde{p}}{\partial t^2} - \tilde{a}^2 \frac{\partial^2 \tilde{p}}{\partial x_j \partial x_j} = \frac{\tilde{a}^2}{L}\left[\left.\frac{\partial (\rho u_3)}{\partial t}\right|_0 - \left.\frac{\partial (\rho u_3)}{\partial t}\right|_L\right] + \frac{\partial \tilde{\rho}}{\partial t}\frac{\partial \tilde{a}^2}{\partial t} + (\gamma - 1)\frac{\partial \tilde{E}}{\partial t} + \tilde{a}^2 \frac{\partial^2 (\tilde{\rho}\tilde{u}_i \tilde{u}_j)}{\partial x_i \partial x_j} \quad (13)$$

The time derivatives of ρu_3 will be determined by the boundary conditions at the injector and nozzle entrance.

C. Injector and Nozzle Boundary Conditions

The mass flux per unit area flowing from the injectors will be considered to be a function of local pressure at the exit of the injector, which is the injector face. Thus, $\rho u_3|_0 = g(p, x_1, x_2)$, in which the function $g(p, x_1, x_2)$ can be determined by an analysis of the flow in the orifice and upstream in the propellant feed system. For portions of the injector face where no orifice hole exists, $g = 0$. Consequently

$$\frac{\tilde{a}^2}{L}\left.\frac{\partial (\rho u_3)}{\partial t}\right|_0 = f(p, x_1, x_2)\frac{\partial p}{\partial t} \quad (14)$$

with the definition $f(p, x_1, x_2) = (\tilde{a}^2/L)\partial g(p, x_1, x_2)/\partial p$. The pressure here is taken at $x_3 = 0$. For the calculations in this paper, oscillatory coupling with the propellant feed system will be neglected (i.e., $\partial g/\partial p = 0$ and $f = 0$).

A special nozzle configuration, which is achievable experimentally, is assumed: a multi-orifice flow exit with each orifice in a perforated plate in the exit plane being a small choked nozzle with a length much shorter than the oscillation wavelength and a residence time much shorter than the oscillation period. Then, the flow through the nozzle is quasi-steady. This nozzle boundary condition for nonlinear transverse waves was developed by Crocco and Sirignano [7,59]. Consider the entrance Mach number of the nozzle to be sufficiently low so that the entrance stagnation values and static values can be assumed to be identical. Also, the boundary condition is abbreviated, neglecting the higher-order effects of the transverse velocity. From this well-known choked-nozzle relation

$$(\rho u_3)_L = \frac{A_{\text{throat}}}{A_{\text{entrance}}}\left(\frac{\gamma}{\mathbf{R}}\right)^{1/2}\left(\frac{\gamma + 1}{2}\right)^{-\frac{\gamma+1}{2(\gamma-1)}}\frac{p}{T^{1/2}} \quad (15)$$

with p_0 and T_0 representing the steady-state values at the nozzle entrance and taking isentropic fluctuations through the nozzle

$$(\rho u_3)_L = \frac{A_{\text{throat}}}{A_{\text{entrance}}}\left(\frac{\gamma}{\mathbf{R}}\right)^{1/2}\left(\frac{\gamma + 1}{2}\right)^{-\frac{\gamma+1}{2(\gamma-1)}}\frac{p_0^{\frac{\gamma-1}{2\gamma}}}{T_0^{1/2}}p^{\frac{\gamma+1}{2\gamma}} = \hat{K}p^{\frac{\gamma+1}{2\gamma}} \quad (16)$$

and, using the preceding definition of $\hat{K}$, one obtains

$$\left.\frac{\partial (\rho u_3)}{\partial t}\right|_L = \hat{K}\frac{\gamma + 1}{2\gamma}\left[p^{\frac{1-\gamma}{2\gamma}}\frac{\partial p}{\partial t}\right]_L = K\left[p^{\frac{1-\gamma}{2\gamma}}\frac{\partial p}{\partial t}\right]_L \quad (17)$$

Now, Eq. (13) may be rewritten

$$\frac{\partial^2 \tilde{p}}{\partial t^2} - \tilde{a}^2 \frac{\partial^2 \tilde{p}}{\partial x_j \partial x_j} = -\frac{\tilde{a}^2 K}{L}\left[p^{\frac{1-\gamma}{2\gamma}}\frac{\partial p}{\partial t}\right]_L + f(p, x_1, x_2)\frac{\partial p}{\partial t} + \frac{\partial \tilde{\rho}}{\partial t}\frac{\partial \tilde{a}^2}{\partial t} + (\gamma - 1)\frac{\partial \tilde{E}}{\partial t} + \tilde{a}^2 \frac{\partial^2 (\tilde{\rho}\tilde{u}_j \tilde{u}_i)}{\partial x_i \partial x_j} \quad (18)$$

The pressure variation in the x_3 direction may be assumed to be minor for many transverse oscillations. The major variation of pressure will be in the transverse direction, as indicated by experimental findings [1] and theory [6,12]. For a pure transverse-wave behavior, there is no acoustical oscillation in the x_3 direction, and so only advection can be expected to produce variations in that flow direction. These variations tend to be slow exponential variations according to the theory. Then, $p_{x_3=0} = p_{x_3=L} = \tilde{p} = p$ and the average designation (i.e., superscript tilde) for pressure can be eliminated. The average designation is also removed for other variables:

$$\frac{\partial^2 p}{\partial t^2} + \left[\frac{a^2 K}{L}(p^{\frac{1-\gamma}{2\gamma}}) - f(p, x_1, x_2)\right]\frac{\partial p}{\partial t} - a^2 \frac{\partial^2 p}{\partial x_j \partial x_j} = \frac{\partial \rho}{\partial t}\frac{\partial a^2}{\partial t} + (\gamma - 1)\frac{\partial E}{\partial t} + a^2 \frac{\partial^2 (\rho u_j u_i)}{\partial x_i \partial x_j} \quad (19)$$

The nozzle boundary condition provides a first time-derivative term, which is a damping function for the oscillation. Some of the energy in the oscillation will be lost by nozzle outflow. The condition at the injector face could be stabilizing or destabilizing, depending on the function $f(p, x_1, x_2)$ resulting from the analysis of the propellant flow system. The term with the time derivative of the energy source E can be described as the forcing function for the oscillation. A combustion model will be developed to relate that quantity E back to pressure, temperature, and velocity. The other two nonlinear terms on the right-hand side of the equation are not dissipative or forcing functions, but they can have a strong influence on the stability, amplitude, and wave shape for the oscillation.

Assume that the averaged pressure, temperature, density, and sound speed will be related by polytropic relations. In this first development, isentropic relations will be used to describe the thermodynamic relations during the oscillation. For transverse oscillations in a cylindrical chamber, shock waves do not form. Also, the acoustic wavelengths are sufficiently long that viscous and diffusive effects are small, except for a combustion zone near an injector. These isentropic relations can be used to eliminate density, sound speed, and temperature from Eq. (19):

$$\frac{\partial^2 p}{\partial t^2} + \left[A p^{\frac{\gamma-1}{2\gamma}} - f(p, x_1, x_2) \right] \frac{\partial p}{\partial t} - B p^{\frac{\gamma-1}{\gamma}} \frac{\partial^2 p}{\partial x_j \partial x_j} = \frac{(\gamma-1)}{\gamma} \frac{1}{p} \left(\frac{\partial p}{\partial t} \right)^2 + (\gamma - 1) \frac{\partial E}{\partial t} + \gamma p^{\frac{\gamma-1}{\gamma}} \frac{\partial^2 (p^{\frac{1}{\gamma}} u_i u_j)}{\partial x_i \partial x_j} \tag{20}$$

in which it is defined that

$$A = \frac{a_0^2 K}{L p_0^{\frac{\gamma-1}{\gamma}}}; \qquad B = \frac{a_0^2}{p_0^{\frac{\gamma-1}{\gamma}}} \tag{21}$$

If a polytropic relation other than the isentropic relation is desired, γ may be replaced by a different constant in the preceding equations.

The neglect of entropy variations in the determination of the pressure and velocity fields is not a very strong assumption. Three arguments can be given. First, pressure is known to be the least sensitive variable to entropy variations. Pressure change travels by acoustic waves, whereas entropy change is carried kinematically by material transport and/or diffused. For example, one cannot detect well by pressure measurements the variation in entropy. Velocity is somewhat more sensitive to entropy variations, but is still dominated by acoustic influence in the combustion-instability case. Temperature and density are more sensitive to entropy variations and kinematic waves. Thus, neglect of entropy waves is not expected to have a direct effect on the pressure waveform. Rather, a theory predicts an indirect effect through interactions at the nozzle; the kinematic wave advects toward the nozzle and causes the reflection of an acoustic wave when it reaches the nozzle.

For subsonic flows in combustion chambers at mean velocities with a low-Mach-number value compared to unity, the acoustic wavelengths are at least one order of magnitude greater than the kinematic wavelengths. Therefore, a second argument is that the shorter kinematic wavelengths produce larger gradients, which result in more susceptiblity to elimination by molecular mixing and turbulent mixing. Surely, the entropy waves can form. Some experimental measurement and verification of kinematic temperature waves exist for combustion chambers with low frequency and relatively low turbulence levels (e.g., solid-propellant T-burners [60]). However, no experimental evidence is known indicating the survival of entropy waves in high-frequency, high-Reynolds-number configurations, such as liquid-propellant rocket motors. As the frequency increases and the mean chamber velocity decreases, the entropy (and, therefore, temperature) wavelength decreases. As the turbulent kinetic energy increases with increasing Reynolds number, the turbulent eddy diffusivity increases. The dissipation time for the kinematic wave can be expected to be proportional to the wavelength squared divided by the turbulent diffusivity, so that time decreases as the frequency and eddy diffusivity increase, and the mean velocity decreases. The travel time of the kinematic wave to the nozzle entrance will increase as the mean velocity decreases. Estimates of these times will show in many practical situations; it can be expected that they will dissipate significantly before reaching the nozzle.

Third, even if mixing were not eliminating the kinematic waves, a length-filtering (i.e., length-averaging) process on the equations to calculate the longer wavelength pressure would remove them from major impact on the pressure solution if the kinematic waves were traveling in the same direction as the acoustic wave. In the present case, with emphasis on transverse waves, the travel of the kinematic waves will primarily be in the x_3 direction, orthogonal to the acoustic wave travel. Therefore, integration over the x_3 direction reduces the effect of those kinematic waves on the equations.

D. Velocity Determination

It remains to determine the averaged velocity by integrating Eq. (2) to obtain the 2-D equation:

$$\frac{\partial(\rho u_i)}{\partial t} + \frac{\partial(\rho u_j u_i)}{\partial x_j} + \frac{\partial p}{\partial x_i} = 0 \tag{22}$$

in which $i = 1, 2$ and $j = 1, 2$. Clearly, the polytropic relations may be used to relate density to pressure in this equation.

A continuity equation for the 2-D averaged variables is also obtained:

$$\frac{\partial \rho}{\partial t} + \frac{\partial(\rho u_j)}{\partial x_j} = 0 \tag{23}$$

By combination of Eqs. (22) and (23), one may write

$$\frac{\partial u_i}{\partial t} + u_j \frac{\partial u_i}{\partial x_j} + \frac{C}{p^{\frac{1}{\gamma}}} \frac{\partial p}{\partial x_i} = 0 \tag{24}$$

in which

$$C = \frac{p_0^{\frac{1}{\gamma}}}{\rho_0} \tag{25}$$

The second-order wave equation (20) for p is coupled with two first-order partial differential equations (PDEs) (24) for u_1 and u_2. These equations form the model system for the wave dynamics. It remains to discuss the relations between velocity and pressure, and between the rate E and other thermodynamic variables and velocity.

Entropy and vorticity are related through the Crocco vorticity theorem. Accordingly, the neglect of entropy waves implies a neglect of vorticity waves. Therefore, a velocity potential function ϕ may be established that has

$$\frac{\partial \phi}{\partial x_i} = u_i \tag{26}$$

and, after a combination of Eqs. (22), (23), and (26), one may obtain

$$\frac{\partial \phi}{\partial t} + \frac{1}{2} \frac{\partial \phi}{\partial x_j} \frac{\partial \phi}{\partial x_j} + \int \frac{1}{\rho} \, \mathrm{d}p = \text{constant} \tag{27}$$

The combination of Eqs. (19), (26), and (27) can lead to a third-order wave equation governing ϕ. This alternative approach will not be used here because it raises the order of the PDE for the wave dynamics, although it eliminates the need to solve three equations.

E. Cylindrical Coordinates and Radial Boundary Condition

It is useful to recast Eq. (20) in cylindrical polar coordinates because of the combustion-chamber shape. The variables r and θ will represent the radial distance from the chamber centerline and the azimuthal position, respectively. The velocity components are u_r and u_θ:

$$\frac{\partial^2 p}{\partial t^2} + \left[A p^{\frac{\gamma-1}{2\gamma}} - f(p, x_1, x_2) \right] \frac{\partial p}{\partial t} - B p^{\frac{\gamma-1}{\gamma}} \left[\frac{\partial^2 p}{\partial r^2} + \frac{1}{r}\frac{\partial p}{\partial r} + \frac{1}{r^2}\frac{\partial^2 p}{\partial \theta^2} \right]$$
$$= \frac{(\gamma-1)}{\gamma}\frac{1}{p}\left(\frac{\partial p}{\partial t}\right)^2 + (\gamma-1)\frac{\partial E}{\partial t} + \gamma p^{\frac{\gamma-1}{\gamma}} \left[\frac{\partial^2 (p^{\frac{1}{\gamma}} u_r^2)}{\partial r^2} + \frac{2}{r}\frac{\partial (p^{\frac{1}{\gamma}} u_r^2)}{\partial r} \right.$$
$$\left. + \frac{2}{r}\frac{\partial^2 (p^{\frac{1}{\gamma}} u_r u_\theta)}{\partial r \partial \theta} + \frac{2}{r^2}\frac{\partial (p^{\frac{1}{\gamma}} u_r u_\theta)}{\partial \theta} + \frac{1}{r^2}\frac{\partial^2 (p^{\frac{1}{\gamma}} u_\theta^2)}{\partial \theta^2} - \frac{1}{r}\frac{\partial (p^{\frac{1}{\gamma}} u_\theta^2)}{\partial r} \right] \tag{28}$$

One may now recast the momentum equation in cylindrical coordinates to obtain

$$\frac{\partial u_r}{\partial t} + u_r \frac{\partial u_r}{\partial r} + u_\theta \frac{1}{r}\frac{\partial u_r}{\partial \theta} - \frac{u_\theta^2}{r} + \frac{C}{p^{\frac{1}{\gamma}}}\frac{\partial p}{\partial r} = 0 \tag{29}$$

and

$$\frac{\partial u_\theta}{\partial t} + u_r \frac{\partial u_\theta}{\partial r} + u_\theta \frac{1}{r}\frac{\partial u_\theta}{\partial \theta} + \frac{u_r u_\theta}{r} + \frac{C}{r p^{\frac{1}{\gamma}}}\frac{\partial p}{\partial \theta} = 0 \tag{30}$$

Consider a solid circular wall at radius $r = R$, that is, no acoustic lining is present. The normal velocity at the wall will be zero, and so the following boundary conditions apply to the system of Eqs. (28–30):

$$u_r(t, R, \theta) = 0; \qquad \frac{\partial p}{\partial r}(t, R, \theta) = \frac{p^{\frac{1}{\gamma}} u_\theta^2}{CR} \tag{31}$$

In the calculations, no acoustic coupling with the injection system will be considered. Therefore, $f = 0$ in Eq. (28), and the mass flux at the injector face is constant with time.

The wave dynamics will be studied first by imposing a postulated monotonically increasing relation between the heat-release rate E and the pressure p. However, focus will occur later on a model of coaxial injection, turbulent mixing, and chemical reaction. This model will be more realistic and will introduce physics and chemistry with characteristic times that will not be short, compared to the period of acoustic oscillation. Therefore, time delays will be introduced.

III. Determination of Heat-Release Rate E with Coaxial Injection

A model is required to relate E to velocity and pressure. The effect is sought of the source term E on driving the acoustic oscillation. In particular, the long wavelength impact of that forcing term must be determined. That term represents the rate of conversion of chemical energy to thermal energy, and will create entropy. Under oscillation, it will create kinematic entropy waves as well as directly modifying the longer-wavelength acoustic oscillations. The model equation has filtered those shorter-length kinematic waves.

The simplification of the constant c_p value for the mixture will be made, and $h = c_p T$. Then, the energy equation becomes

$$\rho \frac{\partial T}{\partial t} + \rho \mathbf{u} \cdot \nabla T - \left(\frac{k}{c_p}\right) \nabla^2 T - \frac{1}{c_p}\frac{\partial p}{\partial t} = \rho \frac{\dot{Q}}{c_p} = \rho \frac{Q}{c_p} \omega_F \tag{32}$$

Approximating an isentropic relationship between pressure and density, and defining $\kappa = T/T_o - (p/p_o)^{(\gamma-1)/\gamma}$, we find

$$\frac{\partial \kappa}{\partial t} + \mathbf{u} \cdot \nabla \kappa - D \nabla^2 \kappa = \frac{Q}{c_p T_o} \omega_F \tag{33}$$

in which we take D to be both the thermal eddy diffusivity and the mass eddy diffusivity. For the gas ambient to the mixing, reacting stream, $\kappa = 0$. Some error is accepted when it is assumed that the isentropic relation for density applies throughout the mixing region; it is a good approximation for the ambient gas.

Consider now the mass diffusion, advection, and chemical reaction for each species. The species continuity equation for each species may be written as follows:

$$\frac{\partial Y_i}{\partial t} + \mathbf{u} \cdot \nabla Y_i - D \nabla^2 Y_i = \omega_i \tag{34}$$

If a one-step chemical reaction with the same diffusivity for fuel and oxygen is used, one can construct a Shvab–Zel'dovich variable $\alpha = Y_F - \nu Y_O$, in which ν is the fuel-to-oxygen-mass stoichiometric ratio, and find

$$\frac{\partial \alpha}{\partial t} + \mathbf{u} \cdot \nabla \alpha - D \nabla^2 \alpha = 0 \tag{35}$$

Similarly, defining $\beta = [Q/(c_p T_o)] Y_F - \kappa$, it can be shown that

$$\frac{\partial \beta}{\partial t} + \mathbf{u} \cdot \nabla \beta - D \nabla^2 \beta = 0 \tag{36}$$

For the gas ambient to the mixing, reacting stream, $\alpha = 0$ and $\beta = 0$.

Consider now a coaxial injector with axisymmetric behavior, in which the dependent variables are functions of t, x, and r. The gaseous oxygen flows from an injector at $x = 0$ for $0 \le r \le R_i$, whereas methane flows through the injector at $x = 0$ for $R_i \le r \le R_o$. An Oseen approximation will be made for the velocity field with uniform velocity $U(t)$ in the x direction. The velocities of both streams are taken to be identical, although they differ in practice. Diffusion in the streamwise direction will be neglected. The diffusivity is approximated as a spatially uniform, temporal function due to turbulence modulation. The estimate is based on the turbulent viscosity approximation for a self-similar turbulent jet [61].

$$\nu_T = \frac{U_0(x) r_{1/2}(x)}{35} \tag{37}$$

in which, in Eq. (37), $U(t)$ is substituted for the centerline velocity $U_0(x)$, and R_o is the jet's half-width. Furthermore, the standard value of 0.7 is used for the turbulent Prandtl number, which yields

$$D = \frac{U(t) R_o}{24.5} \tag{38}$$

The Oseen approximation, eddy-diffusivity approximation, and boundary- or mixing-layer approximation used here are well established in the literature. Variations in the velocity and turbulent diffusivity and diffusion in the main flow direction will cause quantitative corrections, but no qualitative corrections are expected. The approximation implies that the ambient combustion-chamber gas will recirculate and parallel the injected propellants at the same velocity. Equations (35) and (36) become

$$\frac{\partial \alpha}{\partial t} + U(t)\frac{\partial \alpha}{\partial x} - D\left[\frac{\partial^2 \alpha}{\partial r^2} + \frac{1}{r}\frac{\partial \alpha}{\partial r}\right] = 0 \tag{39}$$

and

$$\frac{\partial \beta}{\partial t} + U(t)\frac{\partial \beta}{\partial x} - D\left[\frac{\partial^2 \beta}{\partial r^2} + \frac{1}{r}\frac{\partial \beta}{\partial r}\right] = 0 \tag{40}$$

In addition, we have

$$\frac{\partial Y_F}{\partial t} + U(t)\frac{\partial Y_F}{\partial x} - D\left[\frac{\partial^2 Y_F}{\partial r^2} + \frac{1}{r}\frac{\partial Y_F}{\partial r}\right] = \omega_F \tag{41}$$

The ambient boundary conditions are $\alpha(t, x, \infty) = \beta(t, x, \infty) = Y_F(t, x, \infty) = 0$. Boundary conditions are needed at $x = 0$. Consider that, for $0 \le r \le R_i$, $T(t, 0, r) = T_i(t)$, $Y_O(t, 0, r) = Y_{O,i}(t)$, $Y_F(t, 0, r) = 0$, $\kappa(t, 0, r) = T_i/T_o - (p/p_o)^{(\gamma-1)/\gamma}$, $\alpha(t, 0, r) = -\nu Y_{O,i}(t) \equiv f(t)$, $\beta(t, 0, r) = (p/p_o)^{(\gamma-1)/\gamma} - T_i/T_o \equiv g(t)$. For $R_i \le r \le R_o$, $T(t, 0, r) = T_i(t)$, $Y_O(t, 0, r) = 0$, $Y_F(t, 0, r) = Y_{F,o}(t)$, $\kappa = T_i/T_o - (p/p_o)^{(\gamma-1)/\gamma}$, $\alpha(t, 0, r) = Y_{F,o}$, and $\beta = [Q/(c_p T_o)] Y_{F,o} + (p/p_o)^{(\gamma-1)/\gamma} - T_i/T_o$. For $r \ge R_o$, $Y_O(t, 0, r) = Y_F(t, 0, r) = 0$, $\kappa(t, 0, R) = 0$, $\alpha(t, 0, r) = 0$, and

$\beta(t,0,r) = 0$, in which $p(t,0,r)$ and $T(t,0,r)$ have the ambient values.

The scaling still has the pressure wavelength much larger than the domain under study here; the acoustic wavelength is $O(100$ cm) near the wall, whereas the diffusion layers are of $O(1$ cm), and the reaction zones are even smaller. Thus, the pressure may be considered uniform (over the domain of an individual injector, but varying from one injector to another), although mass fractions and temperature will vary spatially and temporally due to the combined effects of heat and mass diffusion, convection or advection, and compression or expansion. The time for an acoustic wave to propagate through a single-injector region is smaller than or comparable to the time for diffusion and reaction in that region. The wave-speed order of magnitude is 10^2–10^3 m/s over a centimeter or so in transverse dimension for a time between $O(10^{-5}$ s) and $O(10^{-4}$ s); the combustion times are about 10^{-4} s. Therefore, the time variation of pressure is important for the combustion dynamics.

Equations (39–41) have the same linear differential operator with the first two equations being homogeneous. Physically, diffusion is occurring in individual axisymmetric planes that are advecting at velocity $U(t)$ in the x direction. Visualize a continual set of planes perpendicular to the x direction, which advect downstream from the injector face with a temporal diffusion within each of these planes. Thus, one may convert the two first-derivative terms into a Lagrangian time-derivative term. That is, define $\tilde{t} = t - \tau = \int \mathrm{d}x/U$, in which τ is the time when mass in the particular plane was injected. Then, the equations become

$$\frac{\partial \alpha}{\partial \tilde{t}} - D\left[\frac{\partial^2 \alpha}{\partial r^2} + \frac{1}{r}\frac{\partial \alpha}{\partial r}\right] = 0 \tag{42}$$

$$\frac{\partial \beta}{\partial \tilde{t}} - D\left[\frac{\partial^2 \beta}{\partial r^2} + \frac{1}{r}\frac{\partial \beta}{\partial r}\right] = 0 \tag{43}$$

and

$$\frac{\partial Y_F}{\partial \tilde{t}} - D\left[\frac{\partial^2 Y_F}{\partial r^2} + \frac{1}{r}\frac{\partial Y_F}{\partial r}\right] = \omega_F \tag{44}$$

The boundary conditions at $x = 0$ can now be converted to initial conditions. That is, the boundary values at the instant when the element of mass was injected are the initial conditions for the diffusion plane to be solved for each of the planes (perpendicular to the x direction), which continually emerge from the injector face and advect downstream.

The standard Green's function may be used to solve this problem:

$$G(r,\tilde{t};\xi,t') = \frac{1}{4\pi D(\tilde{t}-t')}\exp\left[-\frac{(r-\xi)^2}{4D(\tilde{t}-t')}\right] \tag{45}$$

The solutions to Eqs. (42) and (43) may be written as

$$\alpha(\tilde{t},r) = 2\pi\int_0^\infty G(r,\tilde{t};\xi,0)\alpha(0,\xi)\xi\,\mathrm{d}\xi \tag{46}$$

and

$$\beta(\tilde{t},r) = 2\pi\int_0^\infty G(r,\tilde{t};\xi,0)\beta(0,\xi)\xi\,\mathrm{d}\xi \tag{47}$$

Equation (44) is coupled to the equations for α and β through the reaction rate ω_F, but only in one direction, and so it can be solved sequentially. For convenience, a linear dependence of the reaction rate on the concentration of each reactant is chosen. That is, the potential numerical problems with the negative mass-fraction exponent of the Westbrook–Dryer kinetics [62] is avoided. In particular, the one-step reaction rate is given by

$$\begin{aligned}\omega_F &= \mathbf{A}\rho Y_O Y_F e^{-/\mathbf{R}_u T} \\ &= \frac{\mathbf{A}p_o}{\nu\mathbf{R}T_o}\frac{p}{p_o}\frac{Y_F[Y_F-\alpha]}{(Q/c_pT_o)Y_F - \beta + (p/p_o)^{(\gamma-1)/\gamma}} \\ &\quad\times\exp\left[\frac{\epsilon/\mathbf{R}_u T_o}{(Q/c_pT_o)Y_F - \beta + (p/p_o)^{(\gamma-1)/\gamma}}\right]\end{aligned} \tag{48}$$

in which $\mathbf{A}$ is the preexponential constant, and ϵ is the activation energy. This equation is nonlinear in Y_F, and so numerical integration will be used.

These equations contain two characteristic times: one for mixing and another for chemical reaction. These characteristic times will result in a time lag for the response of heat release to the pressure oscillation. Methane and gaseous-oxygen propellants were chosen with a fuel-to-oxygen-mass mixture ratio equal to 1/4 and an initial injection temperature $T_i = 400$ K. The chemical-kinetic constants are $\mathbf{A} = 2\times10^8$ m^3/kg · s and $\epsilon = 1.25\times10^8$ J/kg · mol. The appropriate preexponential constant was inferred by matching the law of Eq. (48) to the Westbrook–Dryer law at high-density and low-mass-fraction values characteristic of a diffusion flame.

The reaction characteristic time is defined by the formula

$$\tau_R = 1/\omega_F \tag{49}$$

Here, to obtain the parameter value for τ_R, ω_F is evaluated for a stoichiometric mixture of the reactants at $p = 200$ atm and $T = 2000$ K. For the present choice of constants, we have $\tau_R = 1.63\times10^{-4}$ s. The mixing characteristic time is defined by the formula

$$\tau_M = (R_o - R_i)^2/D \tag{50}$$

which, for the definition of D given in Eq. (38), yields a value of $\tau_M = 4.55\times10^{-4}$ s. Note that the values τ_M and τ_R are used to characterize the calculation, but do not appear in the calculation process. Furthermore, the mean chamber-temperature value is roughly halfway between the injected-propellant temperature and the chemical-equilibrium flame temperature.

IV. Numerical Integration

The evolution equations for p, u_r, u_θ, Eqs. (28–30), are solved using a second-order finite difference procedure on a uniform polar grid, with the velocity fields being staggered with respect to the scalar fields. Specifically, the superscripts i, j, and k denote, respectively, the radial position, azimuthal position, and time, and Δr, $\Delta\theta$, and Δt denote, respectively, the radial and azimuthal grid spacings, and the time step. Also, $p^{i,j,k}$ denotes the pressure at $r = (i-0.5)\Delta r$, $\theta = (j-0.5)\Delta\theta$, $t = k\Delta t$. Additionally, $u_r^{i,j,k}$ represents the radial velocity at $r = i\Delta r$, $\theta = (j-0.5)\Delta\theta$, $t = k\Delta t$, and $u_\theta^{i,j,k}$ represents the azimuthal velocity at $r = (i-0.5)\Delta r$, $\theta = j\Delta\theta$, $t = k\Delta t$.

The evolution equation for Y_F, Eq. (30), is solved on multiple nonoverlapping grids, one for each injector, and aligned with that injector's axis, which are 2-D in the r, x coordinates, with θ variation assumed to be negligible due to the injector's small radius relative to the chamber's radius. Then, for the lth injector grid, r_{gl}, x_{gl} denote, respectively, the grid's local radial and axial coordinates, and Δr_{gl}, Δx_{gl} are used to denote the radial and axial grid spacings. $Y_{F,l}^{i,j,k}$ denotes the value of Y_F at $r_{\mathrm{gl}} = (i-0.5)\Delta r_{\mathrm{gl}}$, $x_{\mathrm{gl}} = (j-0.5)\Delta x_{\mathrm{gl}}$, $t = k\Delta t$.

At time step k, the values of $p^{i,j,k-2}$, $p^{i,j,k-1}$, $u_r^{i,j,k-1}$, $u_\theta^{i,j,k-1}$, $Y_F^{i,j,k-1}$ are known, and $p^{i,j,k}$, $u_r^{i,j,k}$, $u_\theta^{i,j,k}$, $Y_F^{i,j,k}$ are calculated. To this end, Eqs. (28–30) and (41) are discretized using the second-order finite differences in space and time. For Eq. (28), the time discretization is centered on $t = (k-1)\Delta t$, so that the first-order time derivatives take the form $\partial p/\partial t|^{i,j,k-1} \approx (p^{i,j,k} - p^{i,j,k-2})/(2\Delta t)$, the second-order derivatives take the form $\partial^2 p/\partial t^2|^{i,j,k-1} \approx (p^{i,j,k} - 2p^{i,j,k-1} + p^{i,j,k-2})/\Delta t^2$, and $p^{i,j,k-1}$ is used, in which p is not differentiated in time.

On the other hand, the time discretizations for Eqs. (29), (30), and (41) are standard Crank–Nicolson, centered on $t = (k - 0.5)\Delta t$, so that, for example, the first-order time derivative for u_r takes the form $\partial u_r/\partial t|^{i,j,k-1/2} \approx (u_r^{i,j,k} - u_r^{i,j,k-1})/\Delta t$, and the terms that are not differentiated with respect to time take the form $u_r|^{i,j,k-1/2} \approx (u_r^{i,j,k} + u_r^{i,j,k-1})/2$. This can be recognized as the Crank–Nicolson scheme, with the exception that, for the convective derivatives in Eqs. (29) and (30), the second-order upwind scheme is used for the spatial derivatives of u_r, u_θ instead of the standard central differences.

The time discretization of Eqs. (29), (30), and (41) leads to an overall implicit discretization, which is solved by the following iterative procedure:

1) Extrapolate $p^{i,j,k}$, $u_r^{i,j,k}$, $u_\theta^{i,j,k}$, $Y_F^{i,j,k}$ from their values at the time levels $k - 1$ and $k - 2$.

2) Solve for $p^{i,j,k}$ from the discretized pressure-wave equation.

3) Perform an explicit iteration (i.e., use the previous values of $u_r^{i,j,k}$, $u_\theta^{i,j,k}$ for the spatial derivatives) on the values of $u_r^{i,j,k}$, $u_\theta^{i,j,k}$ in the discretized momentum equations.

4) Perform an explicit iteration on the values of $Y_{F,l}^{i,j,k}$ in the discretized form of Eq. (41).

5) If the requisite number of iterations has been achieved, proceed to the next step. Otherwise, go back to step 3.

If at least two iterations are used, this time-stepping procedure is second-order accurate.

To achieve stability of the numerical procedure in the limit as $\Delta r \downarrow 0$, in which $\Delta\theta$ and Δt are proportional to Δr, the one-dimensional discrete Fourier transform of $p^{i,j,k}$, $u_r^{i,j,k}$, $u_\theta^{i,j,k}$ is made, and all components with a wavelength lower than Δr (i.e., the high-frequency components close to the origin) are filtered out. This filtering does not diminish the accuracy of the code, and keeps it stable for Δt proportional to Δr, despite the fact that the Courant number in the azimuthal direction, $C = U\Delta t/r\Delta\theta$, may be much greater than 1 close to the centerline. In the absence of filtering, the Courant criterion $C = U\Delta t/r\Delta\theta \leq 1$ will have to be satisfied everywhere in the domain, requiring that Δt scale as $(\Delta r)^2$.

V. Results

Several types of calculations have been made and will be presented here. First, a convenient, monotonically increasing relation between E and p is chosen, and the wave dynamics are analyzed. Then, the coaxial-injector model was used to study the response of the mixing and combustion process to an imposed, defined pressure oscillation. Finally, the coaxial-injector model and the combustion-chamber wave-dynamics model were coupled for a 10-injector design. Each of these three analyses will be discussed in the following subsections.

The ratio of the specific heats $\gamma = 1.30$ has been chosen for the calculations. A chamber diameter of 0.28 m and a chamber length of 0.5 m with mean initial pressure and temperature of 200 atm and 2000 K, respectively, were considered. For the cases studied with full combustion chamber, the mass flow of the propellants at the injector and, in the steady state, at the nozzle is 121 kg/s. In the single-injector study, one-tenth of that value is used. For the full chamber, the ratio for the sum of the cross-sectional areas of the quasi-steady nozzle throats to the cross-sectional area of the cylindrical combustion chamber is 0.115. Consequently, with the chamber-gas temperature at 2000 K in the steady state, the mean-flow Mach number in the chamber is 0.66.

A. Chamber Acoustic Oscillations with Prescribed $E(p)$

The function $E - E_o = Kp_o[\hat{p}^4 - 0.467\hat{p}^3 + 0.03\hat{p}^2 + 0.00008\hat{p}]$, in which $K = 1.25 \times 10^6$ s^{-1} and $\hat{p} = (p - p_o)/p_o$, was chosen. In this study of wave dynamics without coupling to detailed combustion dynamics, no time lags were present, and the same function $E(p)$ was used at all r, θ positions. Later, the detailed combustion dynamics, with time lag and concentration of combustion in the vicinities of injected-propellant streams, will be considered.

Initial conditions were prescribed for pressure and velocity components that matched the traveling first tangential mode. The initial condition involves a steady flow with the superimposed perturbation, and so there is no difference between a disturbance set as an initial condition and one set at a later time to a steady flow. A number of calculations were performed that had varying initial pressure and velocity amplitudes. For a sufficiently large initial amplitude, an oscillatory limit cycle resulted. Figure 3 presents the results for initial amplitudes. The open dots show the initial amplitude, whereas the filled dots show the amplitude after a long time. Below the initial amplitude $\Delta p_0 = 54$ atm, the perturbation decays, and above that value, it grows to a limit cycle of magnitude $\Delta p_F = 213$ atm.

For a low initial amplitude, decay occurs with time, indicating a spontaneous or linear stability. Above the threshold value of 54 atm for the initial pressure amplitude, the oscillation grows to a stable limit cycle with a peak-to-peak amplitude of 213 atm, as shown in Fig. 4. This threshold value indicates that there is an unstable limit cycle at that amplitude value. Therefore, the possibility of nonlinear triggering is demonstrated here. If the initial profile has a larger amplitude than this stable limit cycle, it decays with time to the limit-cycle value. A considerable deviation from a sinusoidal profile can be observed in the limit cycle.

The determination of growth vs decay comes from the balance of two temporal first-derivative terms in Eq. (28): the middle term on the left side of the equality, representing nozzle damping and propellant-injection-system coupling, and the second term on the right side, representing combustion coupling (i.e., energy addition). In the calculations of this paper, propellant coupling is not considered (i.e.,

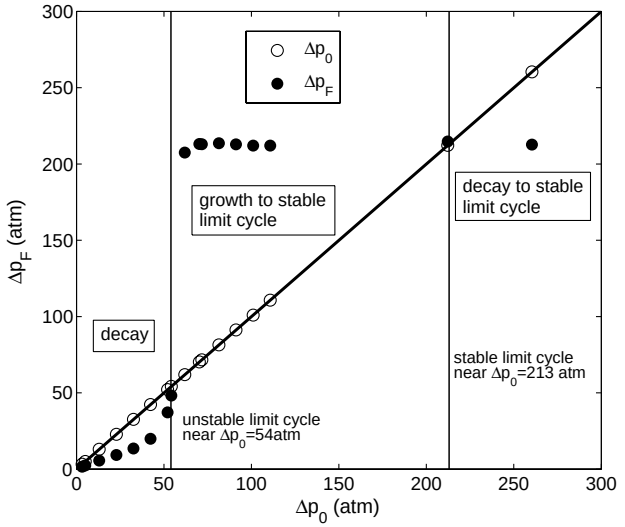

Fig. 3 Final peak-to-peak pressure amplitude vs initial pressure amplitude.

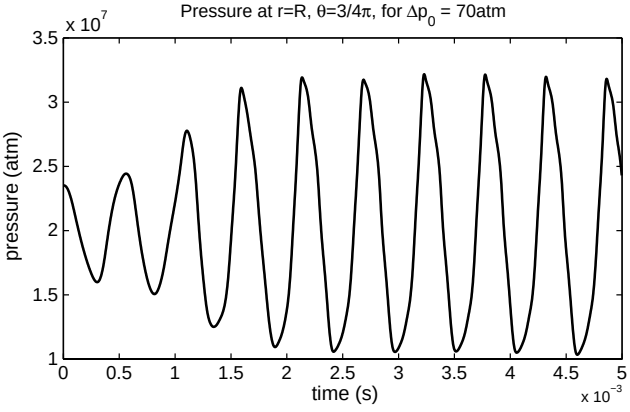

Fig. 4 Pressure history with first tangential initial condition. $r = R$, $\theta = 3/4\pi$, $\Delta p_0 = 70$ atm.

$f = 0$). The nozzle effects, for a quasi-steady short-nozzle case, are always damping. The combustion effects will depend on the time lag, and can be amplifying or damping. In the case of triggering, upon integration over a time period of the oscillation, the amplifying combustion effects exceed in magnitude the nozzle damping if a certain amplitude is exceeded by the initiating disturbance. Thereby, the growth of the amplitude with time occurs until a stable limit is reached. Below that critical amplitude, the nozzle damping dominates in magnitude and the amplitude decays with time until it reaches, after a long (theoretically infinite) time, zero value. The critical amplitude marks the unstable limit cycle. A higher critical amplitude identifies the stable limit cycle. For an initiating amplitude between the two limit-cycle values, growth occurs because combustion dominates. Above the stable limit-cycle amplitude, the nozzle damping again dominates and temporal decay of amplitude would occur, until the oscillation reaches the stable limit.

Figure 5 shows the instantaneous pressure contours for four cases of various initial amplitudes. The wave remains in the general form of a first tangential mode whether growth or decay occurs. The solution with $\Delta p_0 = 5$ atm decays; that solution with $\Delta p_0 = 54$ atm stays approximately the same, and for higher values of Δp_0, the solutions converge to the same limit cycle. Video clips of the pressure wave motion can be found at http://sites.uci.edu/afosrproject/ [63].

B. Sensitivity of Heat Release to Pressure Oscillation

The turbulent mixing and chemical reaction associated with an individual injector were analyzed to determine the heat-release rate per unit volume E as a function of the oscillating pressure. The radius of the outer injector is 1.1 cm, and that of the inner one is 0.898 cm. The methane flows in the annular region with the oxygen flowing through the interior pipe. The fuel and oxidizer leave the injectors with a temperature of 400 K and an axial velocity of 200 m/s. Before the pressure oscillations were imposed, the steady-state behavior was analyzed. The resulting average temperature over the mixing, reacting axisymmetric stream at a constant pressure of 200 atm was determined, upon spatial integration, to be 2000 K. In particular, as a matter of convenience, the inlet temperature was adjusted to give that average value to be the same as the imposed ambient value. Thereby, the average temperature over the mixing and flame zone would also be the average for the full chamber. This value is roughly half of the chemical-equilibrium value. The steady-state temperature contours are shown in Fig. 6. It is seen that a diffusion-flame character exists. Comparisons were made with a steady-state case, in which the Westbrook–Dryer kinetics [62] with nonunity mass-fraction exponents were used. There is no substantial difference in the flame behavior.

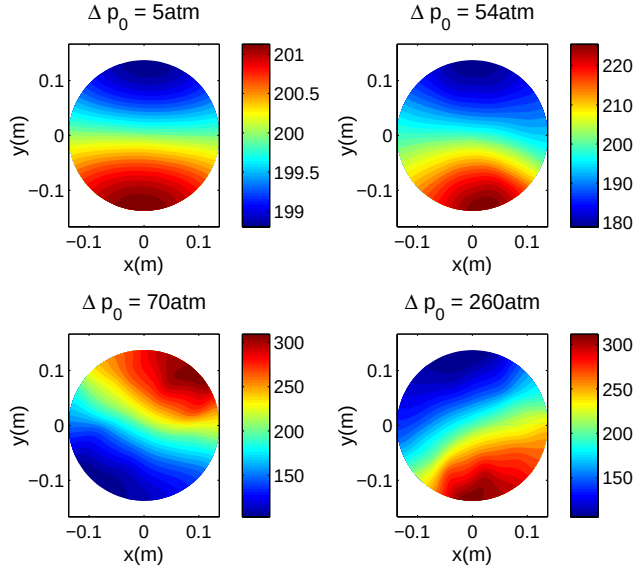

Fig. 5 Four final pressure contours for differing initial perturbations.

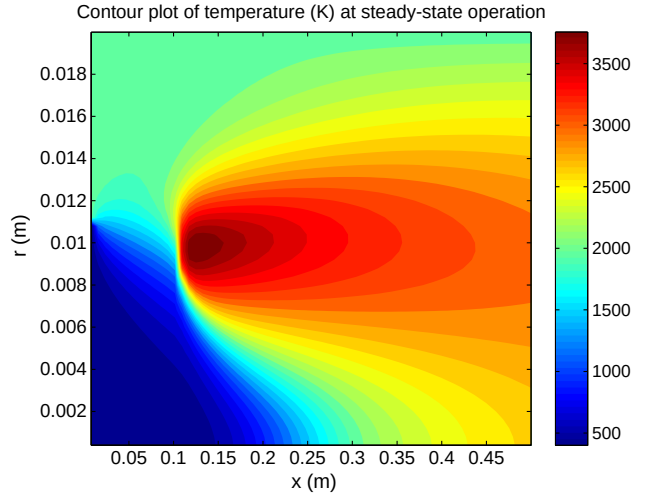

Fig. 6 Steady-state temperature contour; single coaxial injector, stoichiometric methane–oxygen, 200 atm.

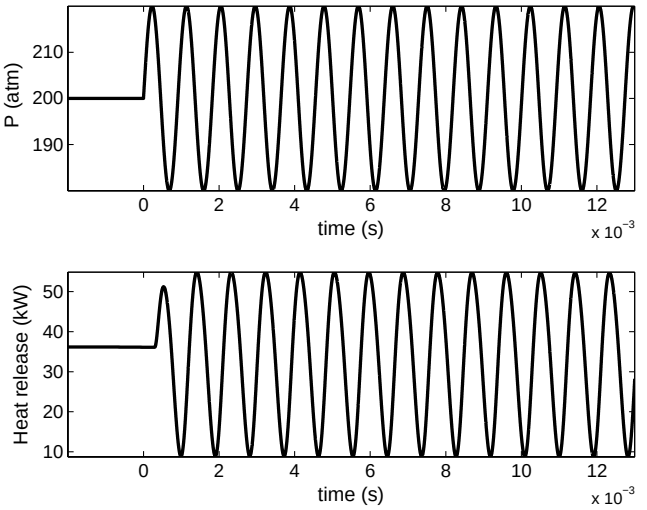

Fig. 7 Single-injector imposed pressure (top) and heat release rate (bottom) histories.

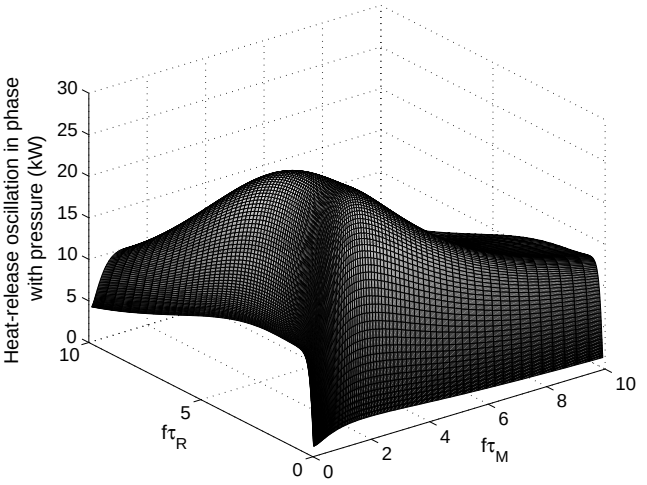

Fig. 8 In-phase, single-injector heat release vs normalized mixing and chemical times.

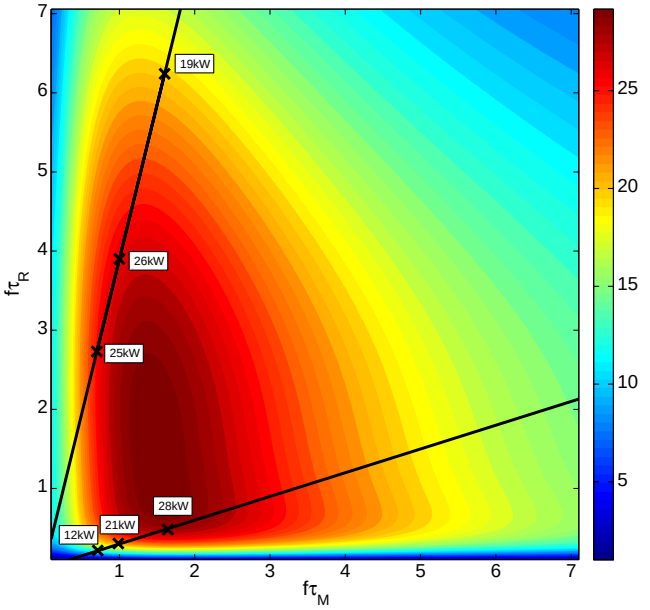

Fig. 9 In-phase, single-injector heat release contours vs normalized mixing and chemical times.

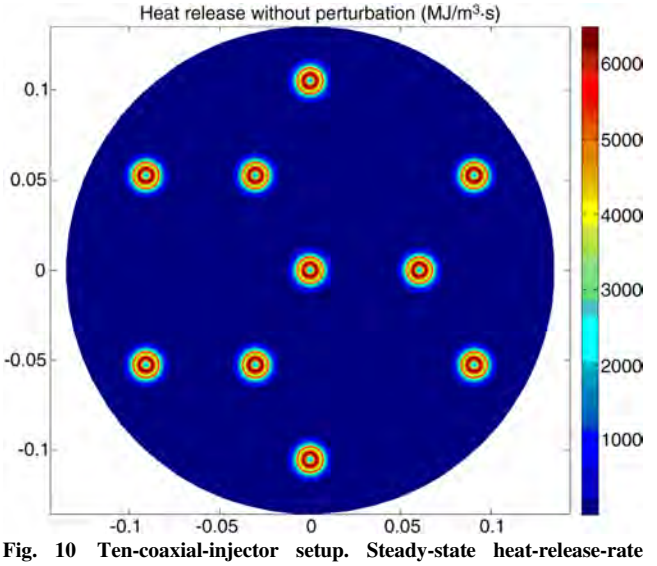

Fig. 10 Ten-coaxial-injector setup. Steady-state heat-release-rate contours.

For the results of an uncoupled single injector portrayed in Figs. 7–9, ω_F was integrated from Eq. (48) over the 3-D (axisymmetric) volume, multiplied by Q (energy per unit mass of fuel), and then divided by the same volume over which the integration occurred. Therefore, essentially, E instantaneously equals the product of Q and the spatial average of ω_F. Here, E is only a function of time.

Two time ratios are key parameters; they are given as the product of frequency f with the characteristic mixing time τ_M, and the product of frequency f with the characteristic chemical-reaction time τ_R. Figure 7 shows one case in which the response of the heat-release rate is sensitive to pressure; a pressure oscillation with the amplitude equal to 10% of the steady-state pressure yields an oscillation in E with an amplitude equal to 25% or so of the steady-state value. A time lag is also found in the heat-release-rate oscillation as expected.

In Fig. 8, the results are given of a survey of the amplitude of E for a given p amplitude as a function of the two ratios, $f\tau_M$ and $f\tau_R$. The 3-D plot shows a peak in a certain region of the parameter space; in particular, the peak domain occurs where both time ratios have magnitudes of order unity. Figure 9 uses contour plots to give the same information as Fig. 8. Now, for the particular choices of propellants (methane and gaseous oxygen) and steady-state operating conditions, the parameters τ_M and τ_R are prescribed, and so, as frequency is varied, the operating state must lie on a straight line in Fig. 9. It is seen that the straight line indicating the operation path passes through the most sensitive region. The lower solid black line represents the domain of $f\tau_M$ and $f\tau_R$ for the present choice of mixing and chemical parameters. That straight line has the operational path passing through the most sensitive region. The symbols tagged to the line, together with the upper line, will be discussed in the next subsection.

C. Wave Dynamics with Combustion for the 10-Injector Design

As the next step, the wave dynamics and the combustion process are coupled. The two characteristic times, τ_M and τ_R, will now affect the feedback of energy from the combustion process to the chamber acoustic oscillation. Also, the combustion and energy feedback will be in certain locations near the injectors.

Ten injectors were considered, as shown in Fig. 10. Six coaxial injectors were placed every $\pi/3$ rad at $r = (3/4)R$, three injectors were placed every $2\pi/3$ rad at $r = (1/2)R$, and one injector was placed at the center. The steady-state pressure and temperature were 200 atm and 2000 K, respectively. E is no longer a simple function of p; rather, it is now a functional dependent on the solution to a set of coupled partial differential equations. Also, the relation is not uniform over the space because the coaxial jets of the 10 injectors do not overlap and the flames where energy is converted do not fill the jets. Using color contours, the figure shows the highly nonuniform magnitude of the energy-release rate E for a steady-state operation.

For the coupled chamber/10-injector analysis, $E = E(t, r, \theta)$ is required; ω_F was taken for each injector as a function of time, downstream distance, and radial distance from the injector centerline; integrated over the axial distance; and divided by the chamber length to get an average over the chamber length. The injector-related position was converted to a chamber radius and an azimuthal-angle position; then, the results from 10 injectors were superimposed to get E at each point in 2-D space and time.

A first tangential mode was imposed as the initial condition. For a small initial amplitude, the oscillation decayed, whereas for initial amplitudes larger than approximately 20 atm, the triggering threshold of an unstable limit cycle was exceeded, and the oscillation amplitude grew toward the value for the stable limit cycle. The limit-cycle behavior was not precisely periodic, as shown by the frequency analysis in Fig. 11. The frequencies 2222, 3703, and 1612 Hz correspond, respectively, to the first tangential, second tangential, and subharmonic frequencies. The first tangential frequency is the largest, and so it is the dominant mode, but nonlinear resonance has

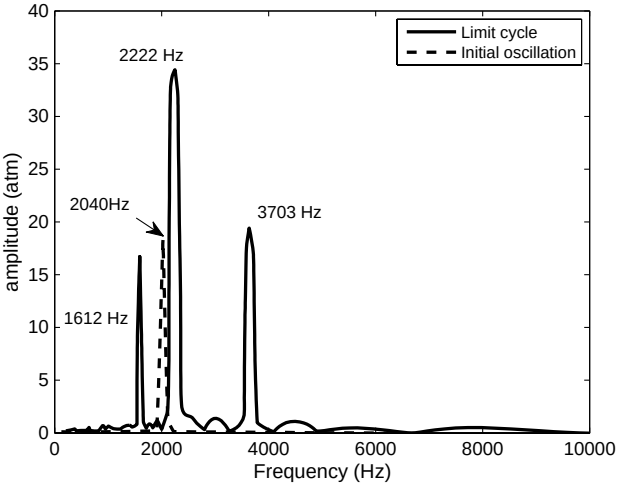

Fig. 11 Ten-injector limit cycle frequency decomposition. First tangential mode initial condition.

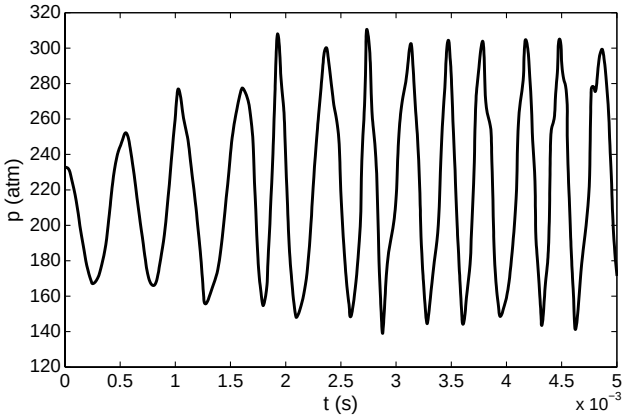

Fig. 12 Ten-injector pressure history. First tangential initial condition. $r = R, \theta = 3/4\pi, \Delta p_0 = 87$ atm.

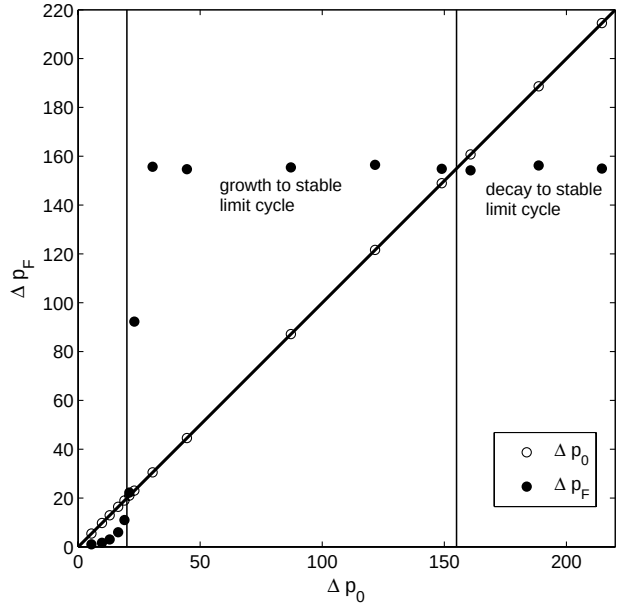

Fig. 13 Final peak-to-peak pressure amplitude vs initial pressure amplitude. Ten-injector setup.

caused two other modes to appear. The second tangential mode appears at a higher frequency, and a subharmonic appears with a frequency approximately equal to the difference between the frequencies of the first tangential mode and the second tangential mode. The potential appearances of such subharmonic modes have been recognized in nonlinear dynamics [64]. The amplitudes for harmonics of the tangential modes are not large, and so the energy from the first tangential mode is being transferred in the nonlinear resonance primarily to the second tangential mode and the subharmonic mode. The tags on the lower line of Fig. 9 indicate the frequencies of the components that appear for the nonlinear resonance. Clearly, the second-tangential-frequency point is located where E is very sensitive.

Figure 12 shows the growth of a typical triggered oscillation with a considerable deviation from a sinusoidal profile in the limit cycle. Figure 13 shows the pressure amplitude after a long time vs the initial pressure amplitude. Below $\Delta p_0 = 20$ atm, the perturbation decays, and above that value, it grows to a limit cycle of magnitude $\Delta p_F = 155$ atm. In Fig. 14, the spatial pressure-amplitude contours are shown after the initial time for a decaying oscillation and for a growing or triggered oscillation. The contour for the triggered oscillation shows deviation from a pure first tangential. See the pressure wave motion at http://sites.uci.edu/afosrproject/ [63].

The frequencies of the first and second tangential modes, and of the subharmonic mode can be seen from Fig. 9 to lie in a sensitive region for the E response to pressure oscillation.

A calculation was made with only the second tangential mode appearing in the initial condition. For a sufficiently large initial disturbance, it grew in amplitude without exciting the first tangential mode or a subharmonic mode. Contour plots of a decaying second tangential solution and one that has converged to the limit cycle can be seen in Fig. 15. Video clips of the wave motion are presented at http://sites.uci.edu/afosrproject/ [63]. Figure 16 shows that, above the critical initial amplitude of $\Delta p_0 = 30$ atm, the amplitude grows to a limit cycle of magnitude $\Delta p_F = 128$ atm. Below $\Delta p_0 = 30$ atm, the perturbation decays.

In Fig. 17, the pressure and energy-release-rate contours can be seen at the same instant of time for the same second-tangential-mode limit cycle. The magnitudes of both p and E are highly nonuniform, the large values of E are confined to the neighborhood of the injector streams, and there is a time lag in the response of E variations to p variations. In the figures at this same instant of time, the time lag for the traveling wave creates a lag in the θ variable.

In addition to the excitation of the second tangential mode, the fourth tangential mode and the second harmonic of the second tangential mode were excited in this solution, as shown in Fig. 18.

For the first tangential mode, further analysis was made by changing the characteristic time τ_R so that the second tangential mode was not in the sensitive region. In that case, the upper line in Fig. 9 describes the operational path. Then, as can be seen in Fig. 18, the first tangential mode and its second and third harmonics appeared without the second tangential mode or a subharmonic mode. The tags on the upper line of Fig. 9 indicate the frequencies of the components that appeared for the nonlinear resonance.

Note that Jacob et al. [19], using a Galerkin method, detected that the nonlinear resonance for a first tangential mode included the development of a second tangential mode. However, they did not allow for the appearance of a subharmonic mode.

Finally, simulations were run with a different initial condition, namely, a Gaussian pulse of half-width 2.5 cm and a peak magnitude $\Delta p_0 = 40$ atm, whose initial direction of travel (at the speed of

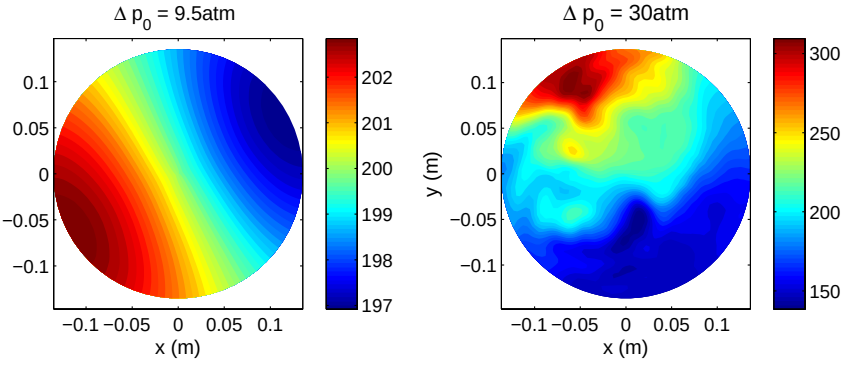

Fig. 14 Pressure contours. Ten-injectors. Decay for $\Delta p_0 = 9.5$ atm. Growth for $\Delta p_0 = 30$ atm.

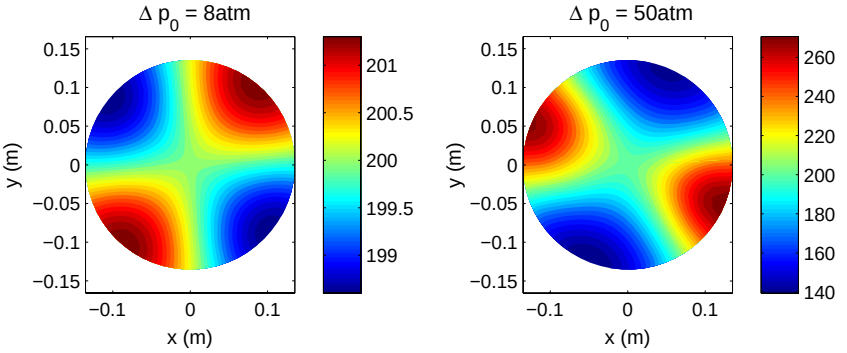

Fig. 15 Pressure contours. Second tangential mode initial condition. Decay for $\Delta p_0 = 8$ atm. Growth for $\Delta p_0 = 50$ atm.

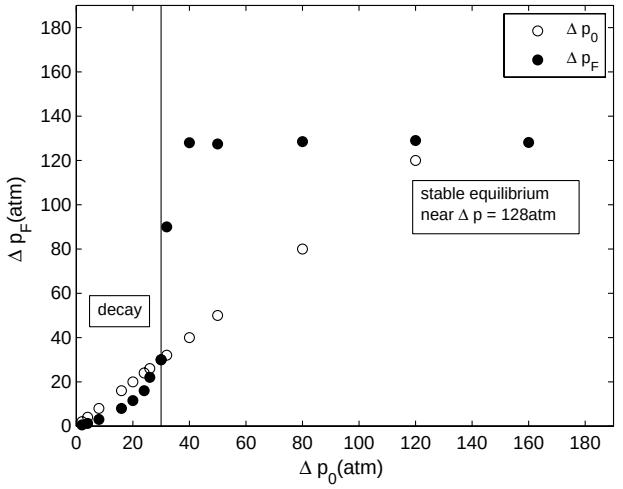

Fig. 16 Final peak-to-peak amplitude vs initial amplitude. Second tangential mode initial condition.

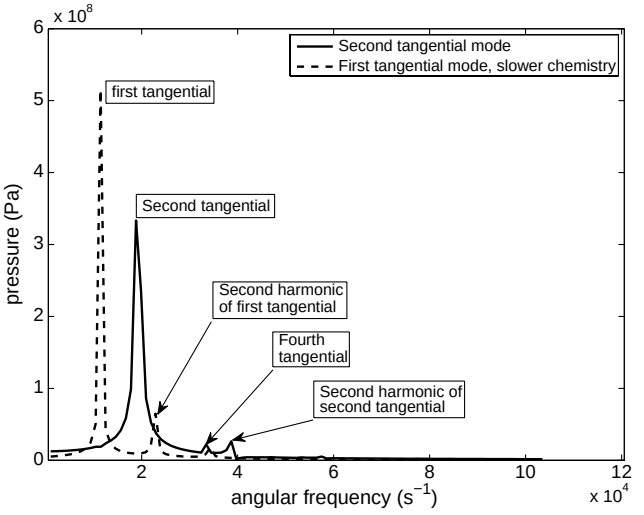

Fig. 18 Frequency decomposition for pressure for two differing initial conditions. $r = R, \theta = 3/4\pi$.

sound) is at an angle θ from the tangent to the chamber wall. See Fig. 19. We show here that the initial perturbation need not be a resonant mode. Of course, any perturbation will have an eigenfunction expansion that includes an infinite number of resonant modes. The initial condition involves a steady flow with the perturbation, and so, again, there is no difference between a disturbance set as an initial condition and one set at a later time to a steady flow. The Gaussian disturbance might be caused by a malfunction in the propellant injection, the combustion processes, or the nozzle outflow. We need not be more specific to observe the consequences here.

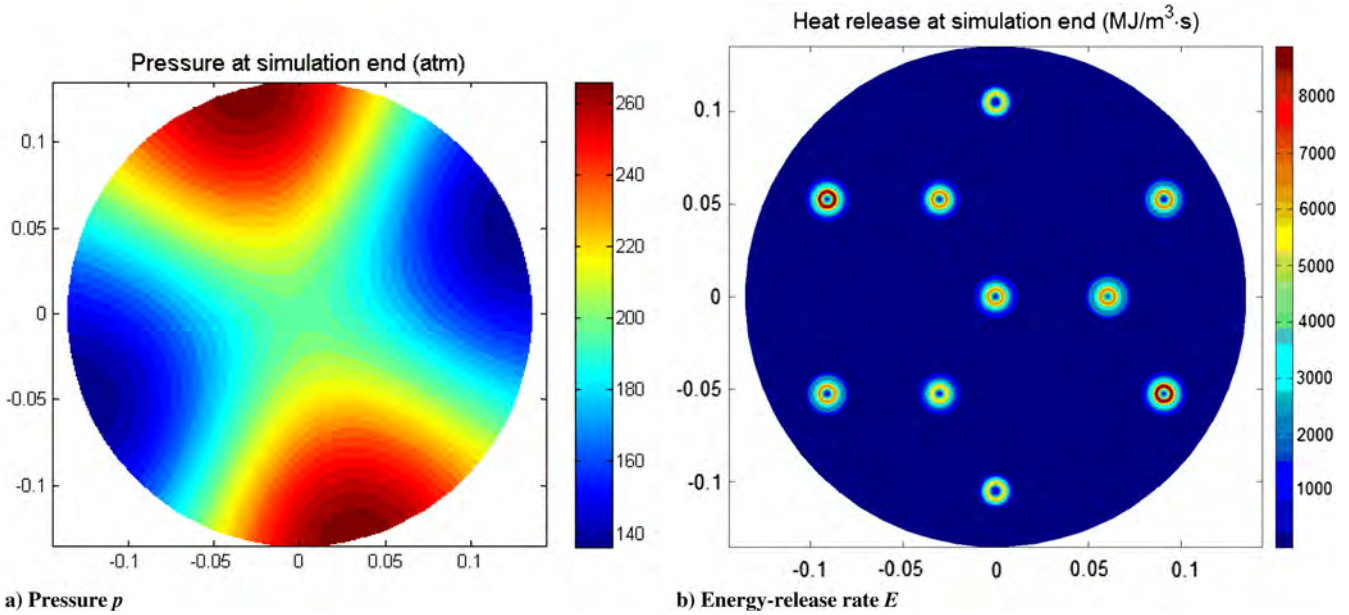

a) Pressure p **b) Energy-release rate E**

Fig. 17 Limit cycle pressure and heat-release contours. Second tangential mode initial condition.

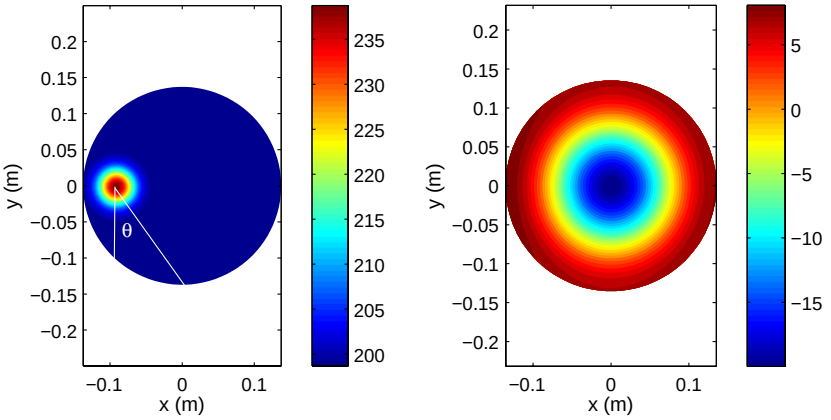

Fig. 19 Initial Gaussian-pressure-pulse simulation can produce radial-mode oscillation.

Figure 20 plots the final amplitudes Δp_F as a function of the angle θ, which varies from 0 to 90 deg from the tangent, the latter value meaning that the pulse is initially moving toward the center of the chamber. As can be seen in Fig. 20, the solution decays for $\theta < 10$ deg, grows to the previously encountered limit cycle at $\Delta p_F = 155$ atm for 10 deg $\leq \theta \leq 43$ deg, and grows to a limit cycle with a higher amplitude of $\Delta p_F = 185$ atm for $\theta > 43$ deg. This higher-amplitude limit cycle is achieved because the first radial mode, with a frequency of 4450 Hz and a higher pressure fluctuation at the location of the interior injectors, is excited (see Fig. 16) and superimposed on the tangential modes, due to the fact that the Gaussian pulse causes high pressure fluctuations at the location of the inner injectors. A video of the wave motion may be found at http://sites.uci.edu/afosrproject/ [63].

The mean pressure changed from 200 atm due to the instability. For the triggered first tangential limit cycle, the presence of the subharmonic mode caused a temporal wobble in the spatially mean limit-cycle pressure, which varied within the limits of from 210.5 to 219.4 atm. The triggered second tangential limit cycle achieved a mean level of 206 atm. These new values for the spatial mean pressure are expected occurrences in nonlinear resonance that have been predicted by the perturbation theory [64].

In this study, the focus is on the triggered instability, and therefore, operational parameter values have been taken, in which the behavior has linear stability with nonlinear unstable and stable limit cycles. However, a few other cases were examined to demonstrate the robustness of the models. Calculations with substantial changes in the mixture ratio from the stoichiometric value to either fuel-rich or fuel-lean situations have produced operations that are linearly stable, but have no unstable and stable limit cycles, and so triggering is not possible at those far-off stoichiometric-mixture ratios. These mixture ratios were modified by varying the radius of the inner channel of the coaxial injector to 0.500 cm for the fuel-rich case, and 1.03 cm for the fuel-lean case. Accordingly, the mean temperature dropped to 1672 and 1851 K, respectively. To maintain the mean pressure at 200 atm, the nozzle-throat-area ratios were changed to 0.076 and 0.124. Another stoichiometric case with increased mass flow and larger throat area produced linearly unstable behavior. Here, the injector areas were doubled and the injection velocity was increased by a $\sqrt{2}$ factor; the area ratio became 0.762. The resulting stable limit-cycle amplitude was 178 atm.

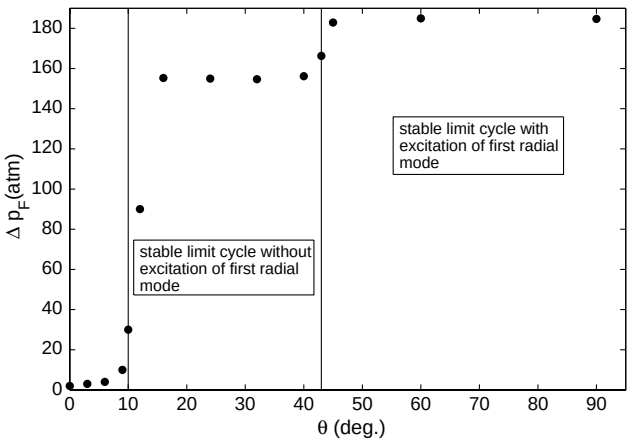

Fig. 20 Final peak-to-peak amplitude vs angle of initial travel.

VI. Conclusions

It has been shown that nonlinear transverse-mode combustion instability in a liquid-propellant rocket motor operating at very high chamber pressure can be studied using a two-dimensional (2-D) model with the radius and azimuthal angle in a circular cylindrical chamber being the critical spatial dimensions. The original three-dimensional equations can be integrated over the axial direction to reduce the dimensionality; variations in that direction are considered to be small. Nonlinear oscillations in the circular cylindrical combustion chamber are allowed with the primary flow direction in the axial direction and the primary wave travel in the transverse directions.

In the first analysis, a monotonically increasing function of pressure was prescribed for the energy-release rate per unit volume E. The function applied uniformly over the 2-D space. Initial conditions were prescribed for the pressure and velocity components that matched the traveling first tangential mode. A number of calculations were performed that had varying initial pressure and velocity amplitudes. For a sufficiently large initial amplitude, an oscillatory limit cycle resulted. For a low initial amplitude, decay occurs with time, indicating a spontaneous or linear stability. Above the threshold value of 54 atm for the initial pressure amplitude, the oscillation grows to a stable limit cycle with a peak-to-peak amplitude of 213 atm, indicating an unstable limit cycle at that amplitude. Therefore, the possibility of nonlinear triggering is demonstrated here. If the initial profile has a larger amplitude than this stable limit cycle, it decays with time to the limit-cycle value. The wave remains in the general form of a first tangential mode whether growth or decay occurs.

A model for turbulent mixing and one-step chemical reaction of methane and gaseous oxygen with coaxial injection has been developed. The analysis of the combustion process associated with an individual injector with an imposed and prescribed pressure oscillation shows that the combustion process has two characteristic times, one for the mixing rate and the other for the chemical-kinetic rate, producing a time lag in the energy-release rate relative to the pressure oscillation. Sensitivity of the amplitude of the energy-release rate to a given pressure amplitude is shown to be largest when the double products of the frequency of oscillation with the characteristic time are of order unity for both τ_R and τ_M.

The coupled combustion process and wave dynamics are calculated for a 10-injector chamber with methane and gaseous oxygen as propellants. Initial conditions with the spatial variation of

the first tangential mode are imposed. Above a certain amplitude for the initial conditions, the amplitude grows; otherwise, it decays with time. Thus, nonlinear triggering is found. Previous predictions of nonlinear triggering involved the use of the sensitive time-lag theory or a comparable heuristic model of the combustion process; this is the first case in which a first-principles combustion analysis yields the triggering prediction.

The second tangential mode develops from the triggering action of the first tangential mode as well. Furthermore, the nonlinear resonance creates a subharmonic mode with a frequency equal to the difference between the two frequencies for these active tangential modes. In this case, the energy from the first tangential mode is primarily transferred to the second tangential mode and the subharmonic mode, with little energy passed to the harmonics of the first tangential mode. Modification of the characteristic combustion times can lead to a triggered instability, in which the triggered first tangential mode transfers energy to its harmonics without the appearance of the second tangential mode or the subharmonic mode. The implication for the use of the Galerkin method (or comparable reduced-basis approaches) is that important errors can occur if the chosen basis functions do not include several natural modes, their harmonics, and certain subharmonics.

The first-tangential-mode instability can also be triggered by local pulses of pressure and velocity with strong sensitivity to the direction of the pulse. For a pulse originating near the outer wall, the likelihood of a triggered instability is increased as the radial component of the pulse direction increases, that is, a tangential mode is triggered at some threshold value of the angle between the direction of the pulse and the tangential direction. Above a larger threshold value of the angle, both a large radial mode and a tangential mode are initiated.

In this analysis, an important extension has been made beyond previous approaches, which used heuristic or empirical (e.g., two-parameter) theories to represent the combustion process. Here, a first-principles combustion analysis has been used to study the nonlinear triggering of the transverse-mode liquid-propellant-rocket-engine (LPRE) instability. The method allows the prediction of the unstable limit cycle, stable limit cycle, and the transient behavior in the parameter domains where nonlinear triggering is possible. Unlike the perturbation methods and Galerkin methods, prior selection of the modes to be analyzed is not required; disturbances with profiles differing from the natural modes can be studied, as the trigger and the consequential unstable modes can be determined.

The streams from the various injectors have been examined, allowing for their partial autonomy, but they have been networked through the wave dynamics. Thereby, a foundation has been provided for a more thorough analysis of the LPRE combustion instability as a stochastic phenomenon in a complex system.

Acknowledgments

This research was supported by the U.S. Air Force Office of Scientific Research under grant FA9550-12-1-0156, with Mitat Birkan as the program manager. The authors acknowledge the helpful discussions on the background material with Athanasios Sideris of the University of California, Irvine; Suresh Menon of Georgia Tech Research Institute; and Douglas Talley of the U.S. Air Force Research Laboratory.

References

[1] Harrje, D., and Reardon, F., "Liquid Propellant Rocket Combustion Instability," NASA SP194, 1972.

[2] Oefelein, J. C., and Yang, V., "Comprehensive Review of Liquid-Propellant Combustion Instabilities in F-1 Engines," *Journal of Propulsion and Power*, Vol. 9, No. 5, 1993, pp. 657–677. doi:10.2514/3.23674

[3] Crocco, L., and Cheng, S.-I., "High Frequency Combustion Instability in Rockets with Distributed Combustion," *Fourth Symposium (International) on Combustion*, Vol. 4, 1953, pp. 865–880.

[4] Crocco, L., and Cheng, S.-I., "Theory of Combustion Instability in Liquid Propellant Rocket Motors," AGARD, Monograph 8, 1956.

[5] Tsien, H. S., "The Transfer Functions of Rocket Nozzles," *ARS Journal*, Vol. 22, No. 3, 1952, pp. 139–143. doi:10.2514/8.4448

[6] Reardon, F. H., Crocco, L., and Harrje, D. T., "Velocity Effects in Transverse Mode Liquid Propellant Rocket Combustion Instability," *AIAA Journal*, Vol. 2, No. 9, 1964, pp. 1631–1641. doi:10.2514/3.2631

[7] Crocco, L., and Sirignano, W. A., "Behavior of Supercritical Nozzle Under Three Dimensional Oscillatory Conditions, AGARDograph No. 117, 1967.

[8] Sirignano, W. A., and Crocco, L., "A Shock Wave Model of Unstable Rocket Combustors," *AIAA Journal*, Vol. 2, No. 7, 1964, pp. 1285–1296. doi:10.2514/3.2534

[9] Sirignano, W. A., "Theoretical Study of Nonlinear Combustion Instability: Longitudinal Mode," Ph.D. Thesis, Rept. No. 677, Dept. of Aerospace and Mechanical Sciences, Princeton Univ., Princeton, NJ, 1964.

[10] Mitchell, C. E., Crocco, L., and Sirignano, W. A., "Nonlinear Longitudinal Instability in Rocket Motors with Concentrated Combustion," *Combustion Science and Technology*, Vol. 1, No. 1, 1969, pp. 35–64. doi:10.1080/00102206908952190

[11] Crocco, L., and Mitchell, C. E., "Nonlinear Periodic Oscillations in Rocket Motors with Distributed Combustion," *Combustion Science and Technology*, Vol. 1, No. 2, 1969, pp. 147–169. doi:10.1080/00102206908952197

[12] Zinn, B. T., "A Theoretical Study of Nonlinear Combustion Instability in Liquid-Propellant Rocket Engines," *AIAA Journal*, Vol. 6, No. 10, 1968, pp. 1966–1972. doi:10.2514/3.4908

[13] Zinn, B. T., and Powell, E. A., "Nonlinear Combustion Instability in Liquid-Propellant Rocket Engines," *Thirteenth Symposium (International) on Combustion*, Vol. 13, No. 1, 1971, pp. 491–503. doi:10.1016/S0082-0784(71)80051-6

[14] Awad, E., and Culick, F., "On the Existence and Stability of Limit Cycles for Longitudinal Acoustic Modes in a Combustion Chamber," *Combustion Science and Technology*, Vol. 46, Nos. 3–6, 1986, pp. 195–222. doi:10.1080/00102208608959800

[15] Yang, V., Kim, S., and Culick, F., "Triggering of Longitudinal Pressure Oscillations in Combustion Chambers, I: Nonlinear Gasdynamics," *Combustion Science and Technology*, Vol. 72, Nos. 4–6, 1990, pp. 183–214. doi:10.1080/00102209008951647

[16] Culick, F., "Some Recent Results for Nonlinear Acoustic in Combustion Chambers," *AIAA Journal*, Vol. 32, No. 1, 1994, pp. 146–169. doi:10.2514/3.11962

[17] Culick, F. E. C., *Unsteady Motions in Combustion Chambers for Propulsion Systems*, AGARDograph AG-AVT-039, 2006.

[18] Flandro, G., Fischbach, S., and Majdalani, J., "Nonlinear Rocket Motor Stability Prediction: Limit Amplitude, Triggering, and Mean Pressure Shift," *Physics of Fluids*, Vol. 19, No. 9, 2007, pp. 094101–094116. doi:10.1063/1.2746042

[19] Jacob, E., Flandro, G. A., Gloyer, P. W., and French, J., "Nonlinear Liquid Rocket Combustion Instability Behavior Using UCDM™ Process," AAIA Paper 2010-6800, July 2010.

[20] Haddad, C. T., and Majdalani, J., "Transverse Waves in Simulated Liquid Rocket Engines," *AIAA Journal*, Vol. 51, No. 3, 2013, pp. 591–605. doi:10.2514/1.J051912

[21] Priem, R. J., and Heidmann, M. F., "Propellant Vaporization as a Design Criterion for Rocket-Engine Combustion Chambers," NASA TR-R-67, 1960.

[22] Heidmann, M. F., and Wieber, P., "Analysis of *n*-Heptane Vaporization in Unstable Combustor with Travelling Transverse Oscillations," NASA TN-3424, 1965.

[23] Strahle, W. C., "Unsteady Laminar Jet Flame at Large Frequencies of Oscillation," *AIAA Journal*, Vol. 3, No. 5, 1965, pp. 957–960. doi:10.2514/3.3024

[24] Strahle, W. C., "Unsteady Reacting Boundary Layer on a Vaporizing Flat Plate," *AIAA Journal*, Vol. 3, No. 6, 1965, pp. 1195–1198. doi:10.2514/3.3103

[25] Strahle, W. C., "High-Frequency Behavior of the Laminar Jet Flame Subjected to Transverse Sound Waves," *Eleventh Symposium (International) on Combustion*, Vol. 11, No. 1, 1967, pp. 747–754. doi:10.1016/S0082-0784(67)80200-5

[26] Strahle, W. C., "Periodic Solutions to a Convective Droplet Burning Problem: The Stagnation Point," *Tenth Symposium (International) on*

Combustion, Vol. 10, No. 1, 1965, pp. 1315–1325. doi:10.1016/S0082-0784(65)80266-1

[27] Sirignano, W. A., *Fluid Dynamics and Transport of Droplets and Sprays*, 2nd ed., Cambridge Univ. Press, New York, 2010, pp. 76–89, 308–313.

[28] Sirignano, W. A., Delplanque, J.-P., Chiang, C., and Bhatia, R., "Liquid Propellant Droplet Vaporization: A Rate-Controlling Process for Combustion Instability," *Liquid Rocket Engine Combustion Instability*, edited by Yang, V., and Anderson, W. E., Vol. 169, Progress in Astronautics and Aeronautics, AIAA, Washington, D.C., 1995, pp. 307–343.

[29] Tong, A., and Sirignano, W. A., "Oscillatory Vaporization of Fuel Droplets in Unstable Combustor," *Journal of Propulsion and Power*, Vol. 5, No. 3, 1989, pp. 257–261. doi:10.2514/3.23146

[30] Bhatia, R., and Sirignano, W. A., "One-Dimensional Analysis of Liquid-Fueled Combustion Instability," *Journal of Propulsion and Power*, Vol. 7, No. 6, 1991, pp. 953–961. doi:10.2514/3.23413

[31] Duvvur, A., Chiang, C.-H., and Sirignano, W. A., "Oscillatory Fuel Droplet Vaporization: Driving Mechanism for Combustion Instability," *Journal of Propulsion and Power*, Vol. 12, No. 2, 1996, pp. 358–365. doi:10.2514/3.24036

[32] Delplanque, J.-P., and Sirignano, W. A., "Numerical Study of the Transient Vaporization of an Oxygen Droplet at Sub- and Super-Critical Conditions," *International Journal of Heat and Mass Transfer*, Vol. 36, No. 2, 1993, pp. 303–314. doi:10.1016/0017-9310(93)80006-G

[33] Delplanque, J.-P., and Sirignano, W. A., "Transcritical Liquid Oxygen Droplet Vaporization: Effect on Rocket Combustion Instability," *Journal of Propulsion and Power*, Vol. 12, No. 2, 1996, pp. 349–357. doi:10.2514/3.24035

[34] Yang, V., and Lin, N. N., "Vaporization of Liquid Oxygen (LOX) Droplets at Supercritical Conditions," *Combustion Science and Technology*, Vol. 97, Nos. 4–6, 1994, pp. 247–270. doi:10.1080/00102209408935380

[35] Nicolis, G., "Physics of Far-From-Equilibrium and Self-Organization," *The New Physics*, edited by Davies, P., Cambridge Univ. Press, Cambridge, England, U.K., 1989.

[36] Langton, C. G., "Computation at the Edge of Chaos: Phase Transitions and Emergent Computation," *Physica D: Nonlinear Phenomena*, Vol. 42, Nos. 1–3, 1990, pp. 12–37. doi:10.1016/0167-2789(90)90064-V

[37] Bak, P., and Chen, K., "Self-Organized Criticality," *Scientific American*, Vol. 264, No. 1, 1991, pp. 46–53. doi:10.1038/scientificamerican0191-46

[38] Bar-Yam, Y., *Dynamics of Complex Systems*, Copernicus Books, New York, 1996.

[39] Kauffman, S., *At Home in the Universe: The Search for Laws of Self-Organization and Complexity*, Oxford Univ. Press, New York, 1996.

[40] Holland, H. J., *Emergence: From Chaos to Order*, Oxford Univ. Press, Oxford, England, U.K., 1998.

[41] Rocha, L. M., "Complex Systems Modeling: Using Metaphors from Nature in Simulation and Scientific Models," *BITS: Computer and Communications News*, Computing, Information, and Communications Division, Los Alamos National Laboratory, Los Alamos, NM, 1999.

[42] Barabasi, A. L., and Albert, R., "Statistical Mechanics of Complex Networks," *Reviews of Modern Physics*, Vol. 74, No. 1, 2002, pp. 47–94. doi:10.1103/RevModPhys.74.47

[43] Wolfram, S., *A New Kind of Science*, Wolfram Media, Champaign, IL, 2002.

[44] Newman, M. E. J., "Power Laws, Pareto Distributions and Zipf's Law," *Contemporary Physics*, Vol. 46, No. 5, 2005, pp. 323–351. doi:10.1080/00107510500052444

[45] Newman, M., *Networks: An Introduction*, Oxford Univ. Press, New York, 2010.

[46] Cohen, R., and Havlin, S., *Complex Networks: Structure, Robustness and Function*, Cambridge Univ. Press, Cambridge, England, U.K., 2010.

[47] Sirignano, W. A., "A Theory of Axial-Mode Shock-Wave Oscillations in a Solid-Rocket Combustor," *Symposium (International) on Combustion*, Vol. 12, No. 1, 1969, pp. 129–137. doi:10.1016/S0082-0784(69)80397-8

[48] Culick, F., "Nonlinear Behavior of Acoustic Waves in Combustion Chambers—I," *Acta Astronautica*, Vol. 3, Nos. 9–10, 1976, pp. 715–734. doi:10.1016/0094-5765(76)90107-7

[49] Oefelein, J., and Yang, V., "Modeling High-Pressure Mixing and Combustion Processes in Liquid Rocket Engines," *Journal of Propulsion and Power*, Vol. 14, No. 5, 1998, pp. 843–857. doi:10.2514/2.5349

[50] Masquelet, M., Menon, S., Jin, Y., and Friedrich, R., "Simulation of Unsteady Combustion in a LOX-GH_2 Fueled Rocket Engine," *Aerospace Science and Technology*, Vol. 13, No. 8, 2009, pp. 466–474. doi:10.1016/j.ast.2009.07.005

[51] Oefelein, J., "Mixing and Combustion of Cryogenic Oxygen–Hydrogen Shear-Coaxial Jet Flames at Supercritical Pressure," *Combustion Science and Technology*, Vol. 178, Nos. 1–3, 2006, pp. 229–252. doi:10.1080/00102200500325322

[52] Tucker, P. K., Menon, S., Merkle, C. L., Oefelein, J. C., and Yang, V., "An Approach to Improved Credibility of CFD Simulations for Rocket Injector Design," AIAA Paper 2007-5572, July 2007.

[53] Tucker, P. K., Menon, S., Merkle, C. L., Oefelein, J. C., and Yang, V., "Validation of High-Fidelity CFD Simulations for Rocket Injector Design," AIAA Paper 2008-5226, July 2008.

[54] Yang, B., Cuoco, F., and Oschwald, M., "Atomization and Flames in LOX/H_2- and LOX/CH_4-Spray Combustion," *Journal of Propulsion and Power*, Vol. 23, No. 4, 2007, pp. 763–771. doi:10.2514/1.26538

[55] Masquelet, M., and Menon, S., "Large Eddy Simulation of Flame-Turbulence Interactions in a Shear Coaxial Injector," *Journal of Propulsion and Power*, Vol. 26, No. 5, 2010, pp. 925–935. doi:10.2514/1.48023

[56] Guézennec, N., Masquelet, M., and Menon, S., "Large Eddy Simulation of Flame-Turbulence Interactions in a LOX-CH_4 Shear Coaxial Injector," AIAA Paper 2012-1267, Jan. 2012.

[57] Schmitt, T., Selle, L., Ruiz, A., and Cuenot, B., "Large-Eddy Simulation of Supercritical-Pressure Round Jets," *AIAA Journal*, Vol. 48, No. 9, 2010, pp. 2133–2144. doi:10.2514/1.J050288

[58] Schmitt, T., Méry, Y., Boileau, M., and Candel, S., "Large-Eddy Simulation of Oxygen/Methane Flames Under Transcritical Conditions," *Proceedings of the Combustion Institute*, Vol. 33, No. 1, 2011, pp. 1383–1390. doi:10.1016/j.proci.2010.07.036

[59] Crocco, L., and Sirignano, W. A., "Effects of the Transverse Velocity Component on the Nonlinear Behavior of Short Nozzles," *AIAA Journal*, Vol. 4, No. 8, 1966, pp. 1428–1430. doi:10.2514/3.3691

[60] Krier, H., Summerfield, M., Mathes, H. B., and Price, E. W., "Entropy Waves Produced in Oscillatory Combustion of Solid Propellants," *AIAA Journal*, Vol. 7, No. 11, 1969, pp. 2079–2086. doi:10.2514/3.5560

[61] Pope, S. B., *Turbulent Flows*, Cambridge Univ. Press, New York, 2000, pp. 99–102, 118–129.

[62] Westbrook, C. K., and Dryer, F. L., "Chemical Kinetic Modeling of Hydrocarbon Combustion," *Progress in Energy and Combustion Science*, Vol. 10, No. 1, 1984, pp. 1–57. doi:10.1016/0360-1285(84)90118-7

[63] UCI AFOSR-Sponsored Research on Liquid-Propellant Rocket Engine Combustion Instability, http://sites.uci.edu/afosrproject/ [retrieved 15 March 2013].

[64] Minorsky, N., *Nonlinear Oscillations*, Van Nostrand, Princeton, NJ, 1962, pp. 462–464, 473–476.

T. Jackson
Associate Editor